



Measurement of the W boson mass

LHCb collaboration[†]

Abstract

The W boson mass is measured using proton-proton collision data at $\sqrt{s} = 13$ TeV corresponding to an integrated luminosity of 1.7 fb^{-1} recorded during 2016 by the LHCb experiment. With a simultaneous fit of the muon q/p_T distribution of a sample of $W \rightarrow \mu\nu$ decays and the ϕ^* distribution of a sample of $Z \rightarrow \mu\mu$ decays the W boson mass is determined to be

$$m_W = 80354 \pm 23_{\text{stat}} \pm 10_{\text{exp}} \pm 17_{\text{theory}} \pm 9_{\text{PDF}} \text{ MeV},$$

where uncertainties correspond to contributions from statistical, experimental systematic, theoretical and parton distribution function sources. This is an average of results based on three recent global parton distribution function sets. The measurement agrees well with the prediction of the global electroweak fit and with previous measurements.

Published in JHEP 01 (2022) 036.

© 2022 CERN for the benefit of the LHCb collaboration. CC BY 4.0 licence.

[†]Authors are listed at the end of this paper.

1 Introduction

The W boson mass (m_W) is directly related to electroweak (EW) symmetry breaking in the Standard Model (SM) [1–3]. At tree level, $m_W = gv/2$ where g is the weak-isospin coupling and v is the vacuum expectation value of the Higgs field. Going beyond tree level the boson masses and couplings receive loop corrections. The value of m_W is related to the precisely measured fine-structure constant (α), the mass of the Z boson (m_Z) and the Fermi constant (G_F), as [4, 5]

$$m_W^2 \left(1 - \frac{m_W^2}{m_Z^2} \right) = \frac{\pi\alpha}{\sqrt{2}G_F} (1 + \Delta), \quad (1)$$

where Δ encapsulates the loop-level corrections. A global fit of EW observables, excluding direct measurements of m_W , yields a prediction of $m_W = 80354 \pm 7$ MeV [6].¹ This can be compared with direct measurements to test for possible beyond SM contributions to Δ in Eq. 1. The 2020 PDG average of direct measurements is $m_W = 80379 \pm 12$ MeV [7]. The sensitivity of the global EW fit to physics beyond the SM is primarily limited by the precision of the direct measurements of m_W [6]. Furthermore, the uncertainty in the prediction is expected to reduce as the top-quark mass, which is the leading source of the parametric uncertainty, is determined more precisely in the future.

The value of m_W was measured to a precision of 33 MeV at the Large Electron-Positron (LEP) collider [8] at CERN and to a precision of 16 MeV in an average [9] of measurements by the CDF [10] and D0 [11] experiments at the Fermilab Tevatron collider. The first measurement at the LHC was performed by the ATLAS collaboration and has an uncertainty of 19 MeV [12]. The hadron collider measurements are based on three observables in leptonic W boson decays, namely the transverse mass, missing transverse momentum and charged lepton transverse momentum (p_T). At hadron colliders, the lepton p_T is measured with good resolution but it is strongly influenced by the W boson transverse momentum distribution, the modelling of which is a potential source of a limiting systematic uncertainty. However, the resolution of the transverse mass is degraded by the pile-up of proton-proton interactions in the same bunch crossing. Therefore, the lepton p_T was the most sensitive observable in the recent measurement performed by the ATLAS collaboration. Despite being based on a small subset of the data recorded to date, the ATLAS measurement of m_W is already limited by uncertainties in modelling W boson production, in particular the parton distribution functions (PDFs) of the proton.

The potential for a measurement based on the muon p_T with the LHCb experiment is studied in Ref. [13] It was estimated that LHCb data collected in LHC Run 2, at a proton-proton (pp) centre of mass energy $\sqrt{s} = 13$ TeV, would allow a measurement with a statistical precision of around 10 MeV. Owing to the complementary pseudorapidity (η) coverage of the LHCb experiment with respect to the ATLAS and CMS experiments, it was demonstrated in Ref. [13] that the PDF uncertainty could partially cancel in an average of m_W measurements by the LHC experiments.

In this paper a first measurement of m_W is presented using $W \rightarrow \mu\nu$ decays, including both W boson and muon charges, collected at the LHCb experiment.² This measurement considers the muon q/p_T distribution, where q is the muon charge. Figure 1 (left) illustrates

¹Throughout this paper natural units with $c = 1$ are used.

²The inclusion of charge-conjugate processes is implied throughout unless otherwise specified.

how the shape of the muon q/p_T distribution in simulated W boson decays is influenced by variations in m_W of ± 300 MeV, which corresponds to roughly ten times the target precision of the present analysis. The q/p_T variable allows all muons with $p_T > 24$ GeV to be visualised; those with $28 < p_T < 52$ GeV are used to determine m_W , while consistent control of the fit can be demonstrated in the region $p_T > 52$ GeV.

The p_T of a muon produced by the decay of a W boson has a strong dependence on the W boson transverse momentum (p_T^W). Direct measurements of the p_T^W distribution have been reported by the ATLAS [14] and CMS [15] collaborations but the intervals are necessarily coarse due to the limited p_T^W resolution. Measurements of the transverse momentum distribution for Z boson production (p_T^Z) are therefore used to validate the predictions for the p_T^W distribution.³ The angular variable ϕ^* [16], defined in Eq. 4, is used in this analysis as a proxy for p_T^Z since its distribution can be measured more precisely than that of p_T^Z . Parton-shower programs such as PYTHIA [17] can be tuned (*e.g.* Ref. [18]) to describe the p_T^Z and ϕ^* data at the per cent level but it is challenging to reliably translate such tunes to W boson production. However, a W -boson-specific tuning of a parton-shower model can be performed simultaneously with a determination of m_W [19].

If electroweak corrections are neglected then the production and leptonic decay of the W boson factorise such that the differential cross-section can be written as

$$\begin{aligned} \frac{d\sigma}{dp_T^W dy dM d\cos\vartheta d\varphi} &= \frac{3}{16\pi} \frac{d\sigma^{\text{unpol.}}}{dp_T^W dy dM} \\ &\left\{ (1 + \cos^2\vartheta) + A_0 \frac{1}{2} (1 - 3\cos^2\vartheta) + A_1 \sin 2\vartheta \cos\varphi \right. \\ &+ A_2 \frac{1}{2} \sin^2\vartheta \cos 2\varphi + A_3 \sin\vartheta \cos\varphi + A_4 \cos\vartheta \\ &\left. + A_5 \sin^2\vartheta \sin 2\varphi + A_6 \sin 2\vartheta \sin\varphi + A_7 \sin\vartheta \sin\varphi \right\}, \end{aligned} \quad (2)$$

where ϑ and φ are the lepton decay angles defined in a suitable frame (the Collins-Soper frame [20] is used in this analysis), and p_T^W , y and M denote the transverse momentum,

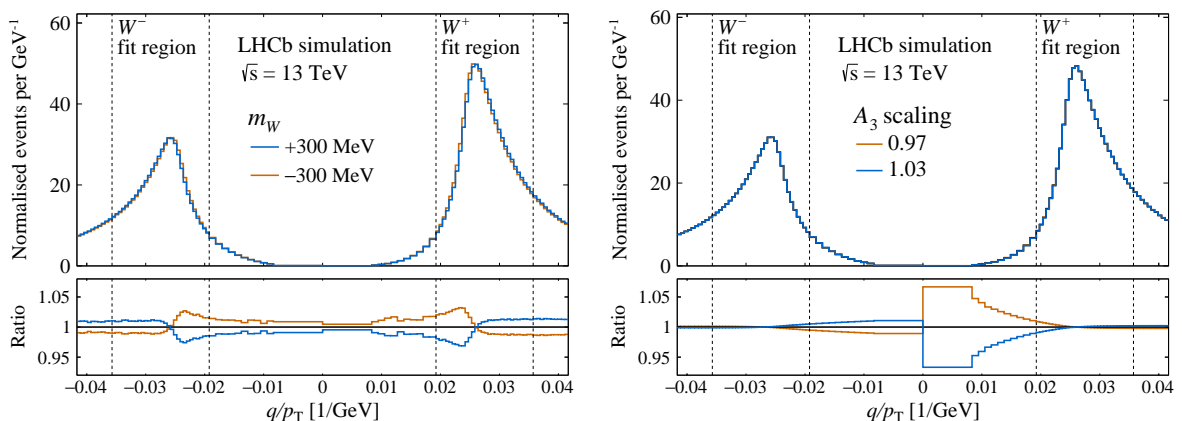


Figure 1: Muon q/p_T distribution in simulated $W \rightarrow \mu\nu$ events with variations in (left) m_W and (right) the A_3 coefficient. The dashed vertical lines indicate the two p_T ranges that are included in the m_W fit.

³For brevity Z denotes Z/γ^* .

rapidity and mass of the final state lepton pair, respectively. An equivalent expression applies to $Z \rightarrow \mu\mu$ production. The eight angular coefficients (A_i) are ratios of helicity cross-sections and depend on p_T^W , y and M ; $\sigma^{\text{unpol.}}$ is usually referred to as the unpolarised cross-section. The coefficients $A_5 - A_7$ are numerically small because they only arise at second order, or higher, in the strong coupling constant (α_s).⁴ The coefficient A_3 is particularly influential on the muon p_T distribution. Figure 1 (right) shows how the q/p_T distribution in simulated W boson events, after the selection requirements described in Sect. 3, changes when A_3 is scaled up and down by 3%.

In this paper, the simulated samples are weighted in the full five-dimensional phase space of vector boson production and decay, using different models for the unpolarised cross-section, angular coefficients, and QED final-state radiation. Several PDF sets are used in the analysis but none of the analysed data were included in the determination of these PDF sets.

This paper is organised as follows. Section 2 describes the data and simulated samples. Section 3 details the signal candidate selection requirements. Section 4 describes charge-dependent curvature corrections that are applied to the data and simulation. The determination of residual smearing corrections to the simulation with a simultaneous fit of $Z \rightarrow \mu\mu$ and quarkonia decays is subsequently described. Section 5 details the measurement of muon selection efficiencies and subsequent weight-based corrections to the simulation. Section 6 describes the treatment of background arising from in-flight decays of light hadrons. Section 7 sets out the modelling of vector boson production and decay. Section 8 describes the simultaneous fit of the model to the muon p_T distribution of W boson candidates and the ϕ^* (defined in Eq. 4) distribution of Z boson candidates to determine m_W . Section 9 explains how results based on three different PDF sets are averaged, and summarises the systematic uncertainties. Several cross-checks of the measurement are reported. The impact of analysis choices and systematic variations on m_W is discussed throughout the paper. The conclusions of the analysis are presented in Sect. 10.

2 Data sets and event selection

The LHCb detector [21, 22] is a single-arm forward spectrometer covering the pseudorapidity range $2 < \eta < 5$, designed for the study of particles containing b or c quarks. The detector includes a high-precision tracking system consisting of a silicon-strip vertex detector surrounding the proton-proton (pp) interaction region [23], a large-area silicon-strip detector located upstream of a dipole magnet with a bending power of about 4 Tm, and three stations of silicon-strip detectors and straw drift tubes [24] placed downstream of the magnet. The tracking system provides a measurement of the momentum, p , of charged particles with a relative uncertainty that varies from 0.5% at low momentum to 1.0% at 200 GeV. The minimum distance of a track to a primary pp collision vertex (PV), the impact parameter, is measured with a resolution of $(15 \oplus 29/p_T) \mu\text{m}$, where p_T is the component of the momentum transverse to the beam, in GeV. Different types of charged hadrons are distinguished using information from two ring-imaging Cherenkov detectors [25]. Photons, electrons and hadrons are identified by a calorimeter system consisting of scintillating-pad and preshower detectors, an electromagnetic calorimeter

⁴Throughout this paper α_s denotes the strong coupling at the scale of the Z boson mass.

and a hadronic calorimeter. Muons are identified by a system composed of alternating layers of iron and multiwire proportional chambers [26]. The online event selection is performed by a trigger [27], which consists of a hardware stage, based on information from the calorimeter and muon systems, followed by a software stage, which applies a full event reconstruction.

This analysis uses a data sample of pp collisions at $\sqrt{s} = 13$ TeV recorded during 2016, corresponding to an integrated luminosity of about 1.7 fb^{-1} . Roughly half of the data were recorded in each of the dipole magnet polarity configurations, resulting in a large degree of cancellation of charge-dependent curvature biases and their associated uncertainties. These data correspond to an average number of proton-proton interactions per bunch-crossing event of $\mathcal{O}(1)$.

During Run 2 the LHCb detector was aligned and calibrated in real-time [28]. The alignment of the tracking system is based on a χ^2 minimisation of the residuals of the clusters of tracker hits evaluated with a Kalman filter that takes into account multiple scattering and energy loss [29]. The alignment algorithm also permits mass and vertex constraints [30]. An optimised offline alignment, which includes $Z \rightarrow \mu\mu$ events with a mass constraint that accounts for the natural width of the Z boson, is used to determine the track parameters. Since the real-time alignment is not optimised for the analysis of high- p_{T} final states, this realignment improves the $Z \rightarrow \mu\mu$ mass resolution by around 30%.

All signal and background processes are simulated using an LHCb specific tune [31] of PYTHIA version 8.186 [17]. The interaction of the generated particles with the detector, and its response, are implemented using the GEANT4 toolkit [32] as described in Ref. [33]. Events are simulated with both polarity configurations and weights are assigned to events in each polarity such that the polarity distribution matches the recorded data.

3 Selection of W boson, Z boson and quarkonia signal candidates

Tracks are identified as muons if they are matched to hits in either three or all four of the most downstream muon stations depending on their momentum. They are then considered in this analysis if they are within the range $1.7 < \eta < 5.0$, and have a momentum of less than 2 TeV. The tracks must have a good fit quality and a relative momentum uncertainty of less than 6%.

Candidate $W \rightarrow \mu\nu$ events are selected online by requiring that one identified muon satisfies the requirements of all stages of the trigger. At the hardware stage a p_{T} of at least 6 GeV is required. The isolation of a muon is defined as the scalar sum of the transverse momenta of all charged and neutral particles, as selected by a particle-flow algorithm, described in Ref. [34], within $(\Delta\eta)^2 + (\Delta\phi)^2 < 0.4^2$ around the muon, where $\Delta\eta$ and $\Delta\phi$ denote the separation in η and azimuthal angle around the beam direction (ϕ), respectively. Hadronic background contributions are suppressed by requiring the muon to have an isolation of less than 4 GeV. For the $W \rightarrow \mu\nu$ selection the η range is tightened to $2.2 < \eta < 4.4$ so that the area of the isolation cone is fully instrumented. The muon must satisfy $\chi_{\text{IP}}^2 < 9$ where χ_{IP}^2 is defined by the difference in the vertex fit χ^2 of the PV with and without including the muon. Background from Z boson events is suppressed by rejecting events that contain a second muon with $p_{\text{T}} > 25$ GeV and an opposite charge

to that of the primary muon candidate. Roughly 2.4 million $W \rightarrow \mu\nu$ candidates are selected in the range $28 < p_T < 52$ GeV.

Candidate $Z \rightarrow \mu\mu$ events are reconstructed from combinations of two oppositely charged identified muons associated to the same PV with an invariant mass within ± 14 GeV of the known Z boson mass [7]. At least one muon must be matched to a single muon selection at all stages of the trigger. Both muons must have $p_T > 20$ GeV, an isolation value below 10 GeV, and an impact parameter significance of less than ten standard deviations. Roughly 190 thousand $Z \rightarrow \mu\mu$ candidates are selected.

Candidate $J/\psi \rightarrow \mu\mu$ and $\Upsilon(1S) \rightarrow \mu\mu$ events, which are primarily used to calibrate the modelling of the momentum measurement, are required to have a pair of oppositely charged identified muons. Both muons must have a transverse momentum above 3 GeV and satisfy a tighter muon identification requirement. In order to specifically select $J/\psi \rightarrow \mu\mu$ candidates originating from b -hadron decays the decay vertices must be displaced from the nearest PV with a significance of at least three standard deviations. These selections retain roughly 1.0 million $\Upsilon(1S) \rightarrow \mu\mu$ candidates and 220 thousand $J/\psi \rightarrow \mu\mu$ candidates.

4 Momentum calibration and modelling

The momentum scale can be precisely determined from the mass measurements of various resonances, including those that decay to muon pairs. However, charge-dependent curvature biases that shift q/p are challenging to estimate because their effect largely cancels in the mass of the resonances. They are also particularly important for the high momentum muons from W and Z boson decays. In Ref. [35] it was proposed to determine corrections using the so-called *pseudomass* variable in $Z \rightarrow \mu\mu$ events

$$\mathcal{M}^\pm = \sqrt{2p^\pm p_T^\pm \frac{p^\mp}{p_T^\mp} (1 - \cos \theta)}, \quad (3)$$

where p^\pm and p_T^\pm are the momenta and transverse momenta of the μ^\pm , respectively. The opening angle between the two muons is denoted θ . Crucially, the value of \mathcal{M}^\pm is independent of the magnitude of the momentum of the μ^\mp and is therefore directly sensitive to curvature biases affecting the μ^\pm candidate. The pseudomass is an approximation of the dimuon mass under the assumption that the dimuon system has zero momentum transverse to the bisector of the two lepton transverse momenta. The ϕ^* observable is defined as [16]

$$\phi^* = \frac{\tan((\pi - \Delta\phi)/2)}{\cosh(\Delta\eta/2)} \sim \frac{p_T^Z}{M}, \quad (4)$$

where $\Delta\phi$ is the azimuthal opening angle between the two leptons and $\Delta\eta$ is the difference between the pseudorapidities of the negatively and positively charged lepton. In events with small values of ϕ^* the pseudomass better approximates the dimuon mass. The pseudomass distributions for events with $\phi^* < 0.05$ are studied in intervals of ϕ and η of the μ^\pm candidate, with a further categorisation into candidates traversing the silicon strip or straw drift tube detectors downstream of the magnet. A maximum likelihood fit of the \mathcal{M}^\pm distributions is performed for each of these detector regions. The signal shapes are described by the sum of a resonant Crystal-Ball [36] component and a nonresonant component represented by an exponential function. The means of the \mathcal{M}^\pm Crystal-Ball

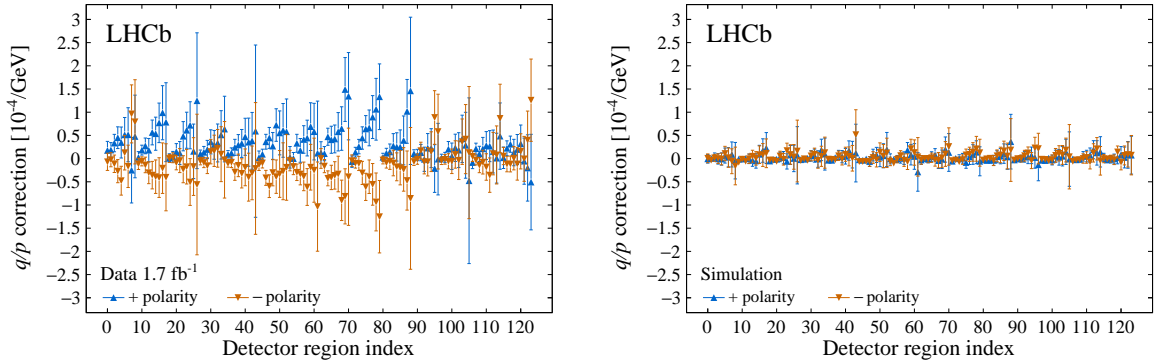


Figure 2: Curvature corrections as a function of the detector region index (depends on η , ϕ and tracking detector, as described in the text) for (left) data and (right) simulation. The corrections are shown for both polarity configurations. The periodic pattern corresponds to a dependence on pseudorapidity that repeats in the intervals of the azimuthal angle.

functions are parameterised as $\bar{M}(1 \pm \mathcal{A})$, where \mathcal{A} and \bar{M} are freely varying asymmetry and mass parameters, respectively. The resulting q/p corrections, which are given by \mathcal{A}/\bar{p} where \bar{p} is the average muon momentum for a given interval in η and ϕ , are presented for the data and simulation for both polarity configurations in Fig. 2.

After the curvature corrections are applied to the data and simulation, the momenta of the simulated muons are smeared to match those in the data, as described below, according to

$$\frac{q}{p} \rightarrow \frac{q}{p \cdot \mathcal{N}(1 + \alpha, \sigma_{\text{MS}})} + \mathcal{N}\left(\delta, \frac{\sigma_{\delta}}{\cosh \eta}\right), \quad (5)$$

where $\mathcal{N}(a, b)$ represents a random number sampled from a Gaussian distribution with mean a and width b . The σ_{MS} and σ_{δ} parameters correspond to the multiple scattering and curvature measurement contributions to the resolution, respectively. The smearing model includes six parameters in total. There are two momentum scale parameters α corresponding to the $2.2 < \eta < 4.4$ region, which coincides with the selection of W boson candidates, and the $\eta < 2.2$ region. A single δ parameter, corresponding to a curvature bias, covers the region $2.2 < \eta < 4.4$, while the value of δ is fixed to zero in the region $\eta < 2.2$. There are two σ_{δ} parameters corresponding to the $2.2 < \eta < 4.4$ and $\eta < 2.2$ regions, while a single σ_{MS} parameter is found to adequately cover all η values. The empirical $1/\cosh \eta$ dependence of the second term in Eq. 5 improves the modelling of the η dependence in the $Z \rightarrow \mu\mu$ mass distribution. As a further correction to Eq. 5, the value of σ_{MS} is increased by a factor of 1.5 in the region $\eta > 3.3$ since this improves the agreement between data and simulation in the η dependence of the quarkonia mass distributions.

The six smearing parameters are determined in a simultaneous fit of $J/\psi \rightarrow \mu\mu$, $\Upsilon(1S) \rightarrow \mu\mu$ and $Z \rightarrow \mu\mu$ candidates in data and simulation. A total of 36 dimuon invariant mass distributions are used in the fit. First, there are three η regions covering $\eta < 2.2$, $2.2 < \eta < 3.3$ and $3.3 < \eta < 4.4$, which result in six categories that depend on the η regions of the two muons. The quarkonia mass distributions are only used in categories with both muons having $\eta > 2.2$. In the subset of the η categories with both muons in $\eta > 2.2$, the $Z \rightarrow \mu\mu$ data are split into three intervals of the asymmetry between the

Table 1: Parameters in the momentum smearing model where the uncertainties quoted are statistical.

Parameter	Fit value
α ($\eta < 2.2$)	$(0.58 \pm 0.10) \times 10^{-3}$
α ($2.2 < \eta < 4.4$)	$(-0.0054 \pm 0.0025) \times 10^{-3}$
δ	$(-0.48 \pm 0.37) \times 10^{-6} \text{ GeV}^{-1}$
σ_δ ($\eta < 2.2$)	$(17.7 \pm 1.2) \text{ keV}^{-1}$
σ_δ ($2.2 < \eta < 4.4$)	$(14.9 \pm 0.9) \text{ keV}^{-1}$
σ_{MS}	$(2.015 \pm 0.019) \times 10^{-3}$

momenta of the two muons, which provides a first order sensitivity to the δ parameters. Finally, all categories are divided by magnet polarity.

As in previous studies of $Z \rightarrow \mu\mu$ production with the LHCb experiment [37], the background under the $Z \rightarrow \mu\mu$ peak is low enough to be neglected but the fit includes exponential functions for the background contributions under the quarkonia resonance peaks. The fractions and slopes of these exponential components vary freely in the fit.

The total χ^2 from the fit is 1862 for 2082 degrees of freedom. Table 1 shows the fit values of the six parameters in the smearing model. The δ values are close to zero as expected given the curvature corrections that have already been applied. Figure 3 shows the dimuon mass distributions for the Z , $\Upsilon(1S)$ and J/ψ samples after combining all categories with both muons in the $2.2 < \eta < 4.4$ range.

The statistical uncertainties in the smearing parameters result in an uncertainty in m_W of 3 MeV. The uncertainty in the world average of the $\Upsilon(1S)$ mass [7] leads to an uncertainty of 2 MeV. The uncertainty in the J/ψ mass is negligible compared to that in the $\Upsilon(1S)$ mass. The $\Upsilon(1S)$ and the Z masses have comparable relative uncertainties but the latter has a negligible effect given the limited size of the Z boson sample. The amount of material in the detector, which affects the modelling of energy losses, is varied by 10%, leading to an uncertainty of 3 MeV. A total uncertainty of 5 MeV is attributed to the shifts in m_W corresponding to: an alternative form of the $1/\cosh \eta$ factor in Eq. 5; and a variation in the η region over which σ_{MS} is scaled. An uncertainty of 2 MeV is attributed to the modelling of the radiative tails in the $\Upsilon(1S)$ and J/ψ simulation, using the methods described in Ref. [38]. The total uncertainty attributed to the modelling of the momentum scale and resolution is 7 MeV.

5 Efficiency corrections

Corrections to the simulation are required for the muon trigger, identification, tracking and isolation efficiencies. The efficiencies are measured using a combination of $Z \rightarrow \mu\mu$ and, in the case of the trigger efficiency, $\Upsilon(1S) \rightarrow \mu\mu$ samples. Positively and negatively charged muons are analysed separately but the results are combined since any charge asymmetries are verified to have a negligible effect.

The trigger efficiency, which accounts for the hardware and software stages, is measured using a combination of $Z \rightarrow \mu\mu$ and $\Upsilon(1S) \rightarrow \mu\mu$ events in which one so-called *tag* muon is required to match a positive decision in the hardware trigger and the first stage of the software-level trigger such that the other muon can be regarded as an unbiased *probe* of

the trigger efficiency. Events are categorised as either *matched* or *unmatched* depending on whether the probe muon is matched to a positive trigger decision in the event data record. The $Z \rightarrow \mu\mu$ sample is verified to be sufficiently pure that the efficiencies can be measured by simply counting the matched and unmatched events with invariant masses within ± 15 GeV of the known Z boson mass [7]. The efficiencies are determined in four uniform ϕ intervals and eight uniform η intervals in the range $2.2 < \eta < 4.4$. There are two additional η intervals in the region $\eta < 2.2$ and one in the region $\eta > 4.4$. The $\Upsilon(1S) \rightarrow \mu\mu$ sample requires background subtraction by fitting the dimuon invariant mass distribution with a parametric model of the signal and background components.

Three p_T intervals, in the range $7.0 < p_T < 12.5$ GeV, are used for the probe muons from $\Upsilon(1S) \rightarrow \mu\mu$ decays while for the $Z \rightarrow \mu\mu$ candidates an adaptive algorithm is employed to determine the p_T intervals. The ratios of the trigger efficiencies in data relative to those in the simulation are shown as a function of $1/p_T$ of the muon in Fig. 4 for each of the intervals in η and ϕ . These are overlaid with a linear function of p_T , from which correction weights for the simulated events are evaluated. The weights for the W boson model only rely on these functions but the weights for the Z boson model also require a parameterisation of the absolute efficiency in the simulation such that the efficiency can be correctly modelled for Z boson candidates with one or two muons matched to a trigger decision. The absolute efficiency is described by an error function that captures the p_T threshold (roughly 6 GeV) of the hardware trigger [28].

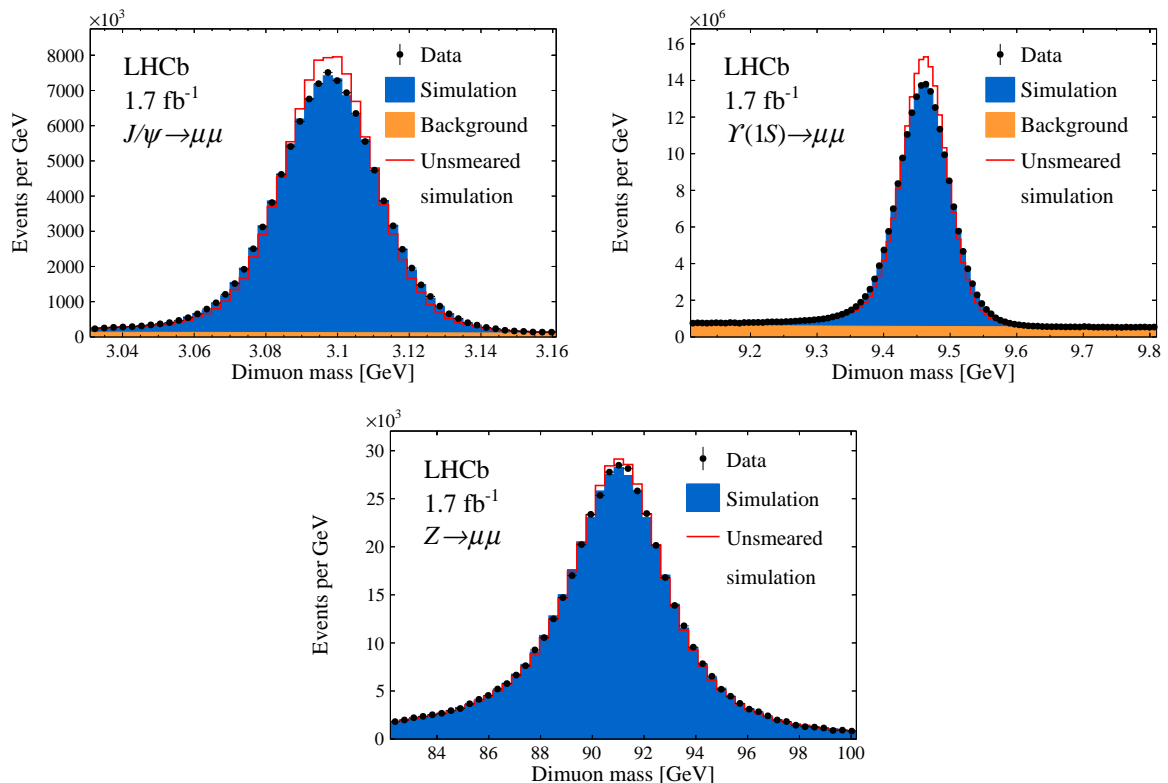


Figure 3: Dimuon mass distributions for selected J/ψ , $\Upsilon(1S)$ and Z boson candidates. All categories with both muons in the $2.2 < \eta < 4.4$ region are combined. The data are compared with the fit model. The red histogram delineates the model before the application of the smearing.

The muon identification efficiency is treated in a similar manner to the trigger efficiencies, using $Z \rightarrow \mu\mu$ events. The resulting event weights, which are applied to the simulated events, are within a few per cent from unity. The tracking efficiency is determined as in previous measurements of W and Z boson production at LHCb [37] using $Z \rightarrow \mu\mu$ candidates where the probe muons are reconstructed by combining hits from the muon stations and the large-area silicon-strip detector located upstream of the magnet [39]. As neither of these detectors are used in the primary track reconstruction algorithms, the probes can be used to measure the tracking efficiency. Correction factors are evaluated using a similar approach to those of the muon identification efficiency, except that the corrections are assumed to be independent of p_T .

The statistical uncertainties in the muon trigger, tracking and identification efficiency corrections are evaluated by rerunning the relevant steps of the analysis, up to and including the m_W determination, with random fluctuations in the underlying efficiency values. The RMS of the resulting variations in the m_W value is regarded as an uncertainty. A systematic uncertainty is attributed to the dependence of the results on the scheme for η and ϕ intervals. This includes restricting to a single interval in ϕ , reducing the number of η intervals (within $2.2 < \eta < 4.4$) by a factor of two, varying the number of p_T intervals between two and ten, and using the simulation rather than the data to control the adaptive algorithm. Further systematic uncertainties are attributed to variations in the isolation and p_T requirements on the tag muons, the mass windows used to determine

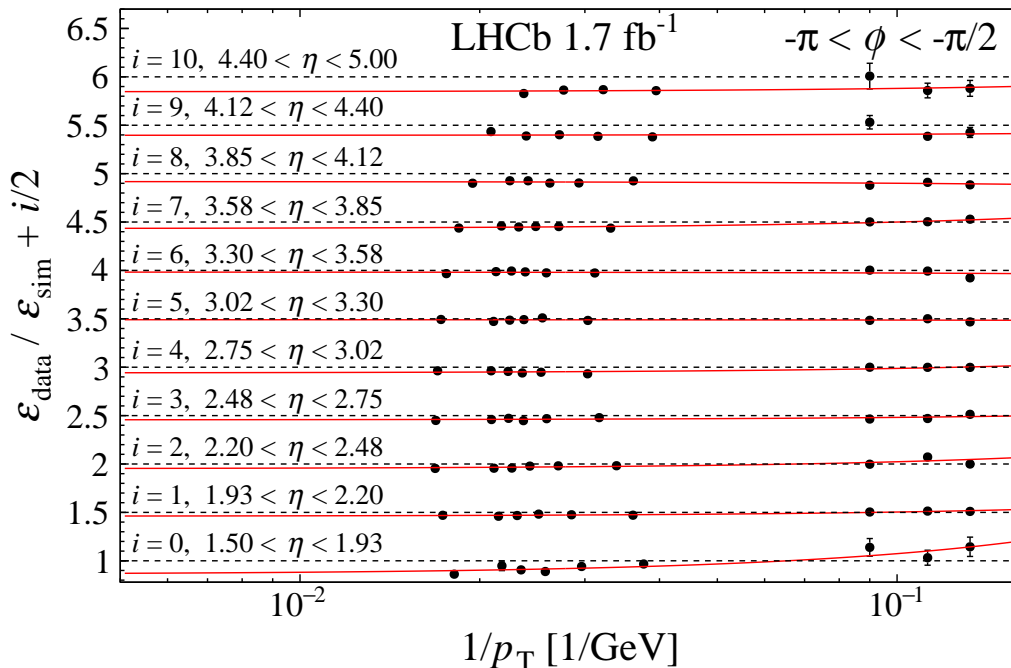


Figure 4: Trigger efficiency ratios in data relative to simulation in intervals of η for a single interval of ϕ . The points are presented as a function of $1/p_T$ and are overlaid with best-fit linear functions of p_T . Points from each η interval are separated for readability by an offset of half the integer index i for that interval. The uncertainties on most of the points are too small for the error bars to be visible.

the $Z \rightarrow \mu\mu$ signal yields, and the functions of the p_T dependence of the efficiency ratios. As the probe muons for the tracking efficiency are reconstructed using minimal tracking information, they have a significantly lower momentum resolution and so a dedicated momentum smearing is applied by default. A variation in the size of this smearing is included in the systematic uncertainty evaluation. The total uncertainty associated to the muon trigger, identification and tracking uncertainties is 6 MeV.

The efficiency of the isolation requirement is measured with $Z \rightarrow \mu\mu$ events. The isolation variable receives contributions from pile-up, the underlying event and the recoil component of the hard process. The *recoil projection* for each muon is defined by

$$u = \frac{\vec{p}_T^V \cdot \vec{p}_T^\mu}{p_T^\mu}, \quad (6)$$

where \vec{p}_T^μ and \vec{p}_T^V are the two-dimensional momentum vectors of the muon and the parent vector boson in the transverse plane. Figure 5 (left) shows the isolation requirement efficiency as a function of u in the $Z \rightarrow \mu\mu$ data and simulation. The efficiency is around 80% at positive values of u where the underlying event contribution dominates. At negative values of u , corresponding to large recoil, the efficiency drops to around 70%. The full reconstruction of the Z boson in $Z \rightarrow \mu\mu$ events allows the determination of corrections as a function of u defined at reconstruction level and consistently applied to W and Z boson events as a function of u defined at generator level, with this approach validated using the Z boson sample. A map of relative efficiencies between data and simulation is determined in intervals of u and η and is used to evaluate weights for the simulated events. Figure 5 (right) shows that the dependence of the isolation efficiency on $1/p_T$ in data is accurately described by the simulation after the corrections. The statistical uncertainties in the isolation efficiency corrections are treated as a source of systematic uncertainty. This is combined in quadrature with a systematic uncertainty that accounts for variations in the u and η intervals and in a smoothing procedure applied to enhance the effective statistical precision of the correction map. The total uncertainty attributed to the isolation efficiency modelling is 4 MeV.

The modelling of the impact parameter and track fit χ^2 variables in simulation is improved in two stages, both of which make use of $Z \rightarrow \mu\mu$ events. Initially, the values of the variables in the simulation are smeared and shifted to match the data. Subsequently, weights are applied to the simulated events to correct for small residual differences in the efficiencies of the selection requirements between data and simulation. In order for the impact parameter modelling to be reliably transported between Z and W boson events, the PVs are refitted with all signal muons removed. The three-dimensional impact parameter is then decomposed into its individual components and these are smeared according to a normal distribution in six intervals in η and seven intervals in ϕ . A similar procedure is used to improve the modelling of the track fit χ^2 distribution. These corrections are followed by smaller corrections applied to account for the efficiencies of the impact parameter and track χ^2 requirements. The efficiency weights are also determined with $Z \rightarrow \mu\mu$ events and are typically within a few per mille from unity. Neither the statistical uncertainties nor reasonable variations in the η and ϕ interval schemes are found to have significant impact on the m_W value. Therefore, no systematic uncertainty is considered.

6 QCD background model

A small background from in-flight decays of pions and kaons into muons is present in the sample of $W \rightarrow \mu\nu$ boson candidates. This background cannot be modelled with high enough accuracy using full detector simulation. It is therefore modelled using a sample of high- p_T tracks, selected by dedicated triggers without muon identification requirements. The W boson selection requirements are applied to this sample but with the muon identification requirement inverted. The resulting sample is verified in simulation to be a pure sample of charged hadrons, composed of roughly 60% pions, 30% kaons and 10% protons, produced directly at the pp interaction vertex. In particular, the impact parameter requirements suppress the heavy flavour hadron content to a negligible level.

The probability of an unstable hadron of mass m , lifetime τ , and momentum p to decay within a detector of length d is

$$1 - \exp\left(-\frac{md}{\tau p}\right) \approx \frac{md}{\tau p}. \quad (7)$$

Similar kinematic distributions are predicted for pions, kaons and protons in the simulation. Therefore, the in-flight decay background can be modelled by the data with weights of $1/p$. The majority of the in-flight decays occur outside the magnetic field region and therefore have minimal influence on the measured momentum. The absolute normalisation is not needed because this background component is allowed to vary freely in the m_W fit.

The weighted p_T spectra for both charges are shown in Fig. 6 and are overlaid with best-fit functions of the form [40],

$$\left(1 + \frac{p_T}{a}\right)^{-n}, \quad (8)$$

where a and n are empirical parameters that are determined in the fits. In addition to giving a good fit to the data, this functional form is verified to describe the pion and kaon spectra in simulation. The fit functions are sampled to generate background candidates

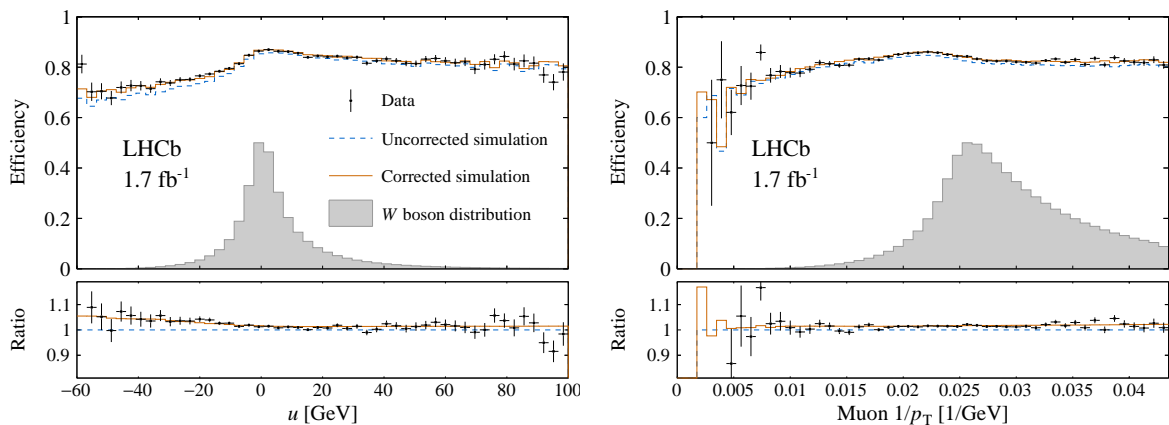


Figure 5: Isolation efficiencies as a function of the observables (left) u and (right) $1/p_T$ of the muon. The grey histograms indicate the, arbitrarily normalised, shapes of each distribution in simulated W boson events. In the lower panels the ratios of the isolation efficiency with respect to the uncorrected simulation are shown.

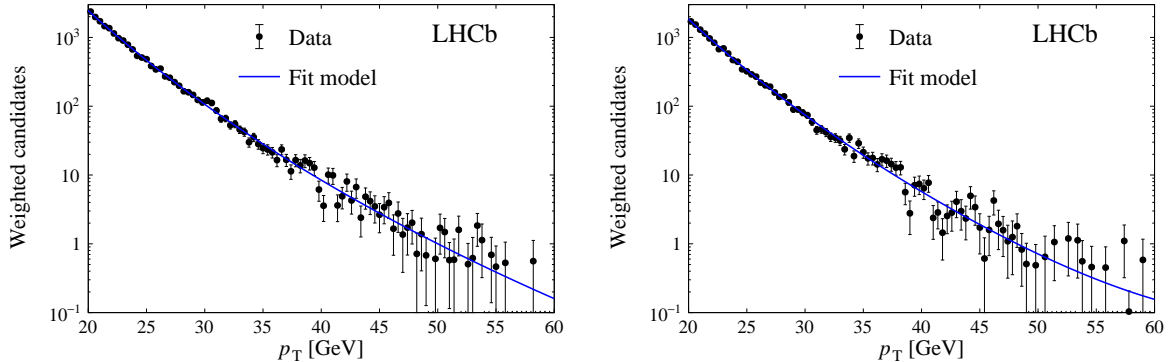


Figure 6: Weighted p_T spectra of the samples of (left) positively and (right) negatively charged hadron candidates. The fit results are overlaid.

for inclusion in the m_W fit. A charge asymmetry of $\mathcal{O}(10\%)$, favouring positively charged hadrons due to the pp initial state, is observed and is included in the sampling.

The uncertainty in the hadronic background model is dominated by systematic sources. Three different systematic uncertainties, which are combined in quadrature, are assessed. The first accounts for assuming that the data sample can be treated as containing a single hadron species. The second accounts for a small bias from the inverted muon identification requirements. The third accounts for a small dependence on the range of p_T values used in the fits to Eq. 8. The combined systematic uncertainty is 2 MeV.

7 Modelling W and Z boson production

The emulation of different m_W hypotheses is achieved by assigning event weights based on a relativistic Breit-Wigner function with a mass-dependent width. Further weight-based corrections are also applied to simulated W and Z boson events to improve upon the limited formal accuracy of PYTHIA. A weighting to model QCD effects is applied in the basis of Eq. 2. A further weighting to model QED effects is applied as a function of the logarithm of the relative energy difference between the dimuon system before and after QED final-state radiation.

Higher order electroweak corrections are not included in the model. Instead, an uncertainty of 5 MeV is attributed to these missing corrections using samples of events generated using POWHEGBoxV2 [41–43] with and without electroweak corrections. These events are interfaced with PYTHIA and the uncertainty is evaluated using the *data challenge* methods described in Sect. 8.1.

7.1 Candidate QCD programs

Five software programs, or combinations of these, are evaluated as potential candidates for the weighting of the simulated W and Z boson events.

1. PYTHIA: Events are generated using PYTHIA version 8.235 [17] with several values of the intrinsic transverse momentum (k_T^{intr}) of the initial state partons and α_s , closely following the work of Ref. [19]. The NNPDF23_1o_as_0130_qed [44] PDFs are

used in the event generation. The events are weighted using the methods described in Ref. [45] to the NNPDF31_lo_as_0118 [46] and CT09MCS [47] PDFs.

2. POWHEGPYTHIA: Events are generated using POWHEGBoxV2 [48] with the NNPDF31_nlo_as_0118 PDFs and are subsequently showered with PYTHIA version 8.244 [17]. The event generation with POWHEGBoxV2 is repeated with different values of α_s . The default Monash [18] tune of PYTHIA is used but event samples are generated with different values of k_T^{intr} , and with the same value of α_s as used in POWHEGBoxV2. This results in a grid of predictions with different α_s and k_T^{intr} values.
3. POWHEGHERWIG: Events are generated equivalently to those from POWHEGPYTHIA but substituting PYTHIA with HERWIG [49] for the parton-shower stage.
4. HERWIG: These events are also equivalent to those of POWHEGPYTHIA except that the hard process and the parton shower are both fully implemented in HERWIG [49].
5. DYTURBO: The cross-sections and angular coefficients are computed at $\mathcal{O}(\alpha_s^2)$ accuracy using DYTURBO [50] with the NNPDF31_nnlo_as_0118 PDFs [46]. Predictions for the unpolarised cross-section include resummation to next-to-next-to-leading logarithms and are produced with several values of the g parameter that controls nonperturbative effects.

Histograms of the unpolarised cross-section in Eq. 2 and the angular coefficients are produced for all combinations of programs and tuning parameters. These histograms, which are used to determine event weights, have intervals in the transverse momentum, rapidity and mass of the vector boson.

7.2 QCD weighting and transverse momentum model

The simulated samples described in Sect. 2 can be weighted in the full five-dimensional phase space of vector boson decays, according to Eq. 2, to provide predictions based on different models of QCD. For the unpolarised cross-section such weights are found by interpolating between the generated histograms described above.

A detailed measurement of the angular coefficients in $pp \rightarrow Z \rightarrow \mu\mu$ at $\sqrt{s} = 8$ TeV was reported by ATLAS [51]. Predictions based on parton showers are generally found to be unreliable in predicting the angular coefficients. However, the ATLAS data are reasonably well described by $\mathcal{O}(\alpha_s^2)$ predictions from DYNNLO [52], on which DYTURBO is based. An exception is the difference between A_0 and A_2 , for which $\mathcal{O}(\alpha_s^2)$ is effectively only leading order, but the present measurement has a negligible sensitivity to this particular detail. Hereafter DYTURBO is used in the modelling of the angular coefficients.

Since the prediction of each angular coefficient relies on separate numerator and denominator calculations, there are four independent renormalisation and factorisation scales that are varied to assess the uncertainty associated with missing higher orders in α_s . In Ref. [53] it is argued that fully correlating the scale variations between the numerator and denominator, which leads to a large degree of cancellation, may result in inadequate uncertainty coverage. The present analysis therefore follows the recommendation of

Ref. [53], which is to vary the four scales independently by factors of $\frac{1}{2}$ and 2 with the constraint that all ratios that could be constructed from the four scales are between $\frac{1}{2}$ and 2. This results in an envelope of 31 values of m_W that sets the associated uncertainty.

Figure 7 compares the p_T^Z distribution in the data with the PYTHIA simulation weighted to the different unpolarised cross-section predictions before and after tuning them to the data. Table 2 lists the χ^2 and the preferred parameter values for the fits with each model. DYTURBO gives a reasonable prediction but overestimates the number of events with large p_T^Z even with tuning of the g parameter. A reasonable initial description is provided by PYTHIA, which is to be expected since it has already been tuned to p_T^Z data. The POWHEGPYTHIA, POWHEGHERWIG and HERWIG predictions poorly describe the shape of the p_T^Z distribution with their default values of $\alpha_s = 0.118$. Their descriptions of the p_T^Z distribution are greatly improved when their α_s and k_T^{intr} parameters are tuned. Of these programs, POWHEGPYTHIA gives the most reliable description of the data, with a preferred α_s value of around 0.125. Large values of α_s are also favoured by other models and in other studies of the p_T^Z distribution [54].⁵ Therefore, POWHEGPYTHIA with freely varying α_s and k_T^{intr} values is selected for the default fitting model. The systematic uncertainty in the description of the p_T^Z and p_T^W shapes is evaluated with alternative predictions from: PYTHIA with the CT09MCS and leading-order NNPDF31 PDFs; HERWIG and POWHEGHERWIG with the next-to-leading-order NNPDF31 PDFs. The envelope of shifts in m_W obtained from using these alternative descriptions is found to be 11 MeV, providing the dominant contribution to the systematic uncertainty associated with the modelling of the vector boson transverse momentum.

All of the event generator predictions can be weighted at leading-order to emulate event generation based on different PDFs. As discussed in Ref. [45] this weighting is not completely valid for events generated at next-to-leading order. Since POWHEGPYTHIA allows *in situ* computation of next-to-leading order PDF weights, it is possible to directly estimate the inaccuracy of the leading-order approximation. With five NNPDF31_nlo_as_0118 replicas it is verified that the differences between the leading-order and next-to-leading-order weighting approaches are smaller than 1 MeV in the m_W fit.

Since it is computationally expensive to determine fully the PDF uncertainty in the DYTURBO angular coefficients, the variations in the next-to-leading order PDFs used in the POWHEGPYTHIA model of the unpolarised cross-section are coherently propagated to the angular coefficients. The DYTURBO angular coefficients are shifted by the differences in values predicted by POWHEGPYTHIA in the default (NNPDF31_nlo_as_0118) PDF compared to the target PDF in the uncertainty assessment.

Separate measurements of m_W based on the NNPDF3.1 [46], CT18 [55] and MSHT20 [56] PDF sets, each with their own PDF uncertainty estimate, are reported. However, since these three sets are based on almost the same data, the central result of this analysis is a simple arithmetic average of the three results, under the assumption that the three PDF uncertainties are fully correlated.

7.3 Angular scale factors

The uncertainties in the angular coefficients from DYTURBO would lead to an uncertainty of $\mathcal{O}(30)$ MeV in m_W , with the dominant contribution attributed to the A_3 coefficient. The

⁵The spread in α_s values between the different models also means that this fit result should not be interpreted as a precise and accurate determination of the value of α_s .

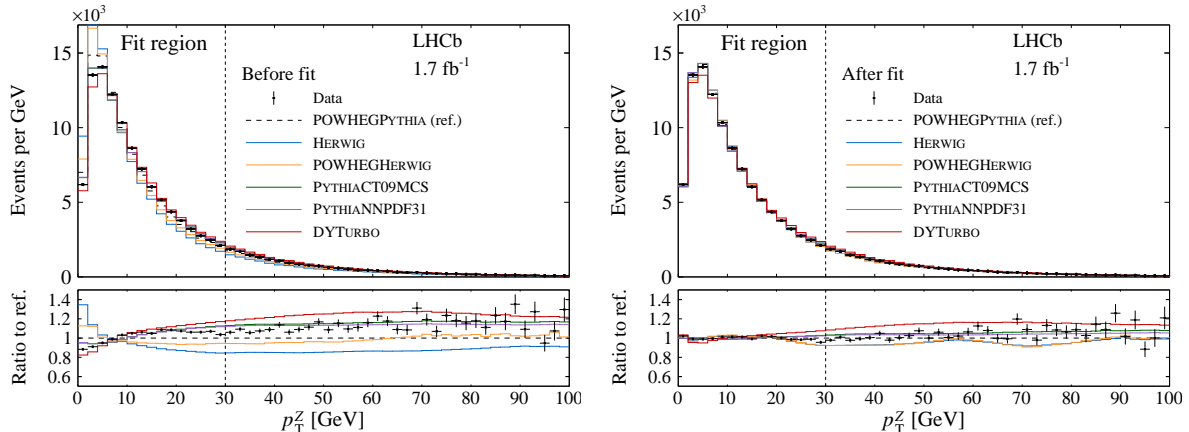


Figure 7: Distributions of p_T^Z (left) before and (right) after the fit for the different candidate models of the unpolarised cross-sections. The fit only considers the region $p_T^Z < 30$ GeV, indicated by the dashed vertical line. In the lower panels the ratios with respect to the POWHEGPYTHIA model are shown.

Table 2: Results of fits of different models to the p_T^Z distribution. The uncertainties quoted are statistical, and the χ^2 comparison of the different models to the data is evaluated considering only statistical uncertainties. The right-hand column lists the fit values of the k_T^{intr} parameter or, for DYTURBO, the analogous g parameter. The fit with DYTURBO has one more degree of freedom than the fits with the other models since only one tuning parameter (g) is used for DYTURBO.

Program	χ^2/ndf	α_s	
DYTURBO	208.1/13	0.1180	$g = 0.523 \pm 0.047 \text{ GeV}^2$
POWHEGPYTHIA	30.3/12	0.1248 ± 0.0004	$k_T^{\text{intr}} = 1.470 \pm 0.130 \text{ GeV}$
POWHEGHERWIG	55.6/12	0.1361 ± 0.0001	$k_T^{\text{intr}} = 0.802 \pm 0.053 \text{ GeV}$
HERWIG	41.8/12	0.1352 ± 0.0002	$k_T^{\text{intr}} = 0.753 \pm 0.052 \text{ GeV}$
PYTHIA, CT09MCS	69.0/12	0.1287 ± 0.0004	$k_T^{\text{intr}} = 2.113 \pm 0.032 \text{ GeV}$
PYTHIA, NNPDF31	62.1/12	0.1289 ± 0.0004	$k_T^{\text{intr}} = 2.109 \pm 0.032 \text{ GeV}$

importance of A_3 can be understood by inspection of Eq. 2: an increase in A_3 enhances the cross-section for events with large $\sin \vartheta$ and $\cos \varphi$. The contribution to the muon p_T from the W boson mass scales with $\sin \vartheta$ while the contribution from the transverse momentum of the W boson scales with $\pm \cos \varphi$ for W^\pm boson production. By allowing a single A_3 scaling factor, which is shared between the W^+ and W^- processes, to vary freely in the m_W fit the angular coefficient uncertainty is reduced by roughly a factor of three, to 10 MeV. Effectively the resulting model only depends on DYTURBO for the kinematic dependence of A_3 , while all other coefficients are fully modelled by DYTURBO.

7.4 Parametric correction at high transverse momentum

While POWHEGPYTHIA is shown in Sect. 7 to describe the p_T^Z distribution in the region below 30 GeV, it systematically underestimates the cross-section at higher p_T^Z . This is expected due to the missing matrix elements for the production of a weak boson and more than one jet. Figure 8 compares the p_T^Z distribution in the data with the model prediction

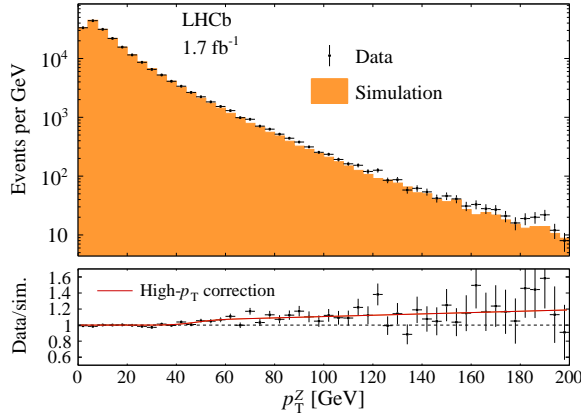


Figure 8: Distribution of p_T^Z compared to the POWHEGPYTHIA model prior to the parametric correction, which is delineated by the red line in the lower panel.

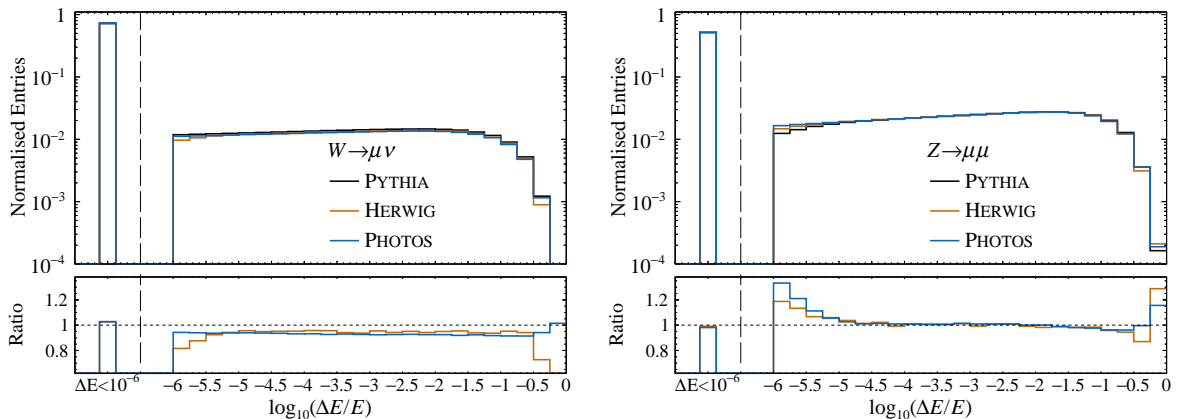


Figure 9: Logarithm of the relative energy loss of the dilepton system due to final-state radiation for (left) W boson events and (right) Z boson events. An energy loss of below 10^{-6} is considered unresolvable and is accounted for in the underflow bin to the left of the dashed vertical line. In the lower panel the ratio with respect to PYTHIA is shown.

having set α_s and k_T^{intr} to be close to the final fit values. For $p_T^Z \geq 40$ GeV the model starts to underestimate the cross-section, reaching the ten per cent level at $p_T^Z \sim 100$ GeV. In the lower panel of Fig. 8 the data to prediction ratio is overlaid with a function of the form

$$(1 + p_0 + p_0 \text{Erf}(p_1(p_T^V - p_2))) \times (1 + p_3 p_T^V). \quad (9)$$

Since the universality of this correction between W and Z boson processes is not well controlled, an uncertainty of 100% of this correction is included as an additional systematic uncertainty associated with the vector boson p_T model. This contributes an uncertainty in the m_W value smaller than 1 MeV.

7.5 QED weighting

The effect of the QED final-state radiation is largely characterised by the energy difference between the final-state lepton system before and after radiation. The logarithm of this

energy difference as described by PYTHIA, HERWIG, and an alternative configuration of PYTHIA with the final-state radiation modelled by PHOTOS [57] is shown in Fig. 9. Event-by-event weights are evaluated for the HERWIG and PHOTOS models relative to PYTHIA and applied to the simulated samples used in the analysis. The default model uses the arithmetic average of the HERWIG, PHOTOS and PYTHIA weights, where the PYTHIA weights are equal to unity. The systematic uncertainty, amounting to 7 MeV, is taken from the envelope of m_W values corresponding to each of the three models taken individually.

8 W boson mass fit

The m_W value is determined through a simultaneous fit of the q/p_T distribution of W boson candidates and the ϕ^* distribution of Z boson candidates. The ϕ^* variable is preferred over p_T^Z because it is less susceptible to several of the modelling uncertainties, while still being sensitive to the parameters affecting the predicted p_T^Z and p_T^W distributions. The ϕ^* distribution extends to $\phi^* = 0.5$ while the q/p_T distribution includes two fit regions covering $28 < p_T < 52$ GeV. Projections of the q/p_T distribution cover a wider interval with $p_T > 24$ GeV that includes regions outside the fit. The model of both distributions is based on simulated event samples with event-by-event weights. The fit minimises the sum of two negative log-likelihood terms, associated with the q/p_T and ϕ^* distributions, that are computed using the Beeston-Barlow-Lite prescription [58], which accounts for the finite size of the simulated samples. The sum of these terms multiplied by a factor of two is denoted as the χ^2 .

The ϕ^* distribution is modelled including background contributions from $Z \rightarrow \tau\tau$ and top quarks. The model of the q/p_T distribution includes the dominant $W \rightarrow \mu\nu$ signal component and several background sources. The largest background, with a fraction of around 7×10^{-2} , is attributed to $Z \rightarrow \mu\mu$, which is simulated with true invariant masses above 20 GeV. The $W \rightarrow \tau\nu$ and hadronic background components each contribute at the $\mathcal{O}(10^{-2})$ level. A combination of rarer background sources including $Z \rightarrow \tau\tau$, top quarks, vector boson pairs, and heavy flavour hadrons gives a total contribution below 10^{-2} .

The fractions of the W^+ and W^- signal components and the hadronic background are allowed to vary freely. The $W \rightarrow \tau\nu$ component is constrained, using the known $\tau \rightarrow \mu\nu\bar{\nu}$ branching fraction [7], relative to the $W \rightarrow \mu\nu$ component. All other component fractions are fixed relative to the observed number of Z boson candidates in the ϕ^* distribution using the fiducial cross-sections for the corresponding processes relative to that of Z boson production. The fiducial selections for W and Z boson processes are the same as used in measurements of the corresponding cross-sections [59]. For all other processes the fiducial regions correspond to the requirement of a single muon in the region $p_T > 20$ GeV and $2 < \eta < 4.5$. The measured cross-section for $Z \rightarrow \mu\mu$ is used [37]. The cross-sections for the rare background processes are determined using POWHEG with the next-to-leading-order NNPDF3.1 PDF sets.

The shapes of background components arising from the decay of electroweak bosons are determined from the same models used to describe the signal component. Systematic variations of the model used to describe W boson production therefore also simultaneously provide systematic variations associated with the shapes of background contributions from the decay of electroweak bosons. The uncertainty in m_W from varying the predicted

cross-sections for the rarer background within their uncertainties is negligible.

The default physics model is based on the simulated samples set out in Sect. 2, fully weighted using a combination of POWHEGPYTHIA and DYTURBO for the QCD description and a combination of PYTHIA, PHOTOS and HERWIG for the QED description. The fit is configured to determine the following parameters:

1. the value of m_W ,
2. the fraction of W^+ signal,
3. the fraction of W^- signal,
4. the fraction of QCD background,
5. the value of α_s for the Z boson processes (α_s^Z),
6. an independent α_s value that is shared for the W^+ and W^- signals (α_s^W),
7. a shared k_T^{intr} value for all W and Z boson processes,
8. and an A_3 scale factor that is shared by the W^+ and W^- signals.

8.1 Data challenge tests

In Sect. 7 it is concluded that POWHEGPYTHIA describes the p_T^Z distribution, in the $p_T^Z \leq 30$ GeV region, better than the other candidate models. It is important to demonstrate that the fit can reliably determine m_W if W boson production is better described by one or more of the other models. Several pseudodata samples are prepared in which the underlying PYTHIA events, without detector simulation, are weighted to match the default DYTURBO and POWHEGPYTHIA model but with the p_T^V distribution modified to match an alternative model. The m_W fit is configured with a simplified model, without background components, using a statistically independent sample of the same PYTHIA events without detector simulation. Figure 10 shows the resulting q/p_T and ϕ^* distributions of these pseudodata samples. Variations of up to five per cent are seen in the shape of the ϕ^* distribution. Within the fit regions in q/p_T variations of several per cent can be seen, while the variations exceed $\mathcal{O}(10^{-1})$ in the high- p_T control region. However, the fit model is able to absorb these differences in the α_s and k_T^{intr} nuisance parameters with variations in the preferred m_W value of no more than 10 MeV. Table 3 lists the results of the fits to these pseudodata samples. The observed variation in m_W is consistent with the uncertainty due to modelling the vector boson transverse momentum distribution in the fit to LHCb data, as discussed in Sect. 7.

8.2 Fit results

The fit to the data, with the NNPDF31_nlo_as_0118 PDF set, returns a total χ^2 of 105 for 102 degrees of freedom. Figure 11 compares the q/p_T and ϕ^* distributions from the data with the fit model overlaid. The model is in good agreement with the data within the fit ranges but it underestimates the high- p_T control region of the q/p_T distribution by up to ten per cent. This underestimation is within the band of modelling uncertainty, which is dominated by the high- p_T^V parametric correction in that region. The values of the eight

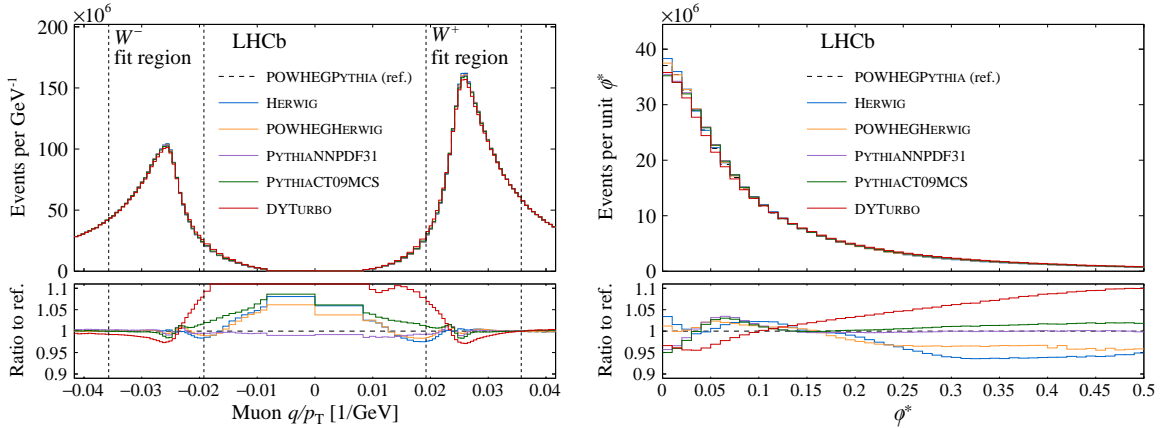


Figure 10: Projections of the (left) q/p_T and (right) ϕ^* distributions for the challenge datasets. The four dashed vertical lines indicate the two fit regions in the q/p_T distribution.

Table 3: Fit results with the same default fit model used for the templates but with different models used for the pseudodata. The POWHEGPYTHIA pseudodata correspond to $\alpha_s = 0.125$ and $k_T^{\text{intr}} = 1.8$ GeV. The HERWIG and POWHEGHERWIG pseudodata correspond to $\alpha_s = 0.136$ and $k_T^{\text{intr}} = 1.3$ GeV. The PYTHIA pseudodata correspond to $\alpha_s = 0.127$ and $k_T^{\text{intr}} = 2.7$ GeV. The DYTURBO pseudodata correspond to $\alpha_s = 0.118$ and $g = 1$ GeV². The contributions to the total χ^2 from the q/p_T and ϕ^* distributions are denoted χ_W^2 and χ_Z^2 , respectively. The shift in the m_W value with respect to the POWHEGPYTHIA pseudodata is denoted δm_W . The uncertainties quoted are statistical.

Data config.	χ_W^2	χ_Z^2	δm_W [MeV]	α_s^Z	α_s^W	A_3 scaling
POWHEGPYTHIA	64.8	34.2	–	0.1246 ± 0.0002	0.1245 ± 0.0003	0.979 ± 0.029
HERWIG	71.9	600.4	1.6	0.1206 ± 0.0002	0.1218 ± 0.0003	1.001 ± 0.029
POWHEGHERWIG	64.0	118.6	2.7	0.1206 ± 0.0002	0.1226 ± 0.0003	0.991 ± 0.029
PYTHIA, CT09MCS	71.0	215.8	–2.4	0.1239 ± 0.0002	0.1243 ± 0.0003	0.983 ± 0.029
PYTHIA, NNPDF31	66.9	156.2	–10.4	0.1225 ± 0.0002	0.1223 ± 0.0003	0.967 ± 0.029
DYTURBO	83.0	428.5	4.3	0.1305 ± 0.0001	0.1321 ± 0.0003	0.982 ± 0.028

parameters determined from the fit are listed in Table 4. The α_s value for the W boson events is roughly 0.002 higher than for the Z boson events. If the fit is configured with a shared α_s value for the W and Z boson events the value of m_W changes by +39 MeV but the χ^2 is increased by more than 20 units, which strongly favours the configuration with independent α_s values. Furthermore, similar variations between the α_s values for W and Z boson events are found in the data challenge tests, as shown in Table 3. The A_3 scaling factor is statistically consistent with unity, which suggests that the $\mathcal{O}(\alpha_s^2)$ predictions from DYTURBO, with the central scale choices, are compatible with the data.

Figure 12 (left) shows the projection of the q/p_T distribution in the Z boson sample, where the final state muon is only included if it satisfies the W boson selection requirements. The model is in good agreement with the data. Figure 12 (right) shows that the Z boson rapidity distribution is well described by the model.

Table 4: Values of the parameters determined in the m_W fit with the NNPDF31_nlo_as_0118 PDF set. The uncertainties quoted are statistical.

Parameter	Value
Fraction of $W^+ \rightarrow \mu^+ \nu$	0.5288 ± 0.0006
Fraction of $W^- \rightarrow \mu^- \nu$	0.3508 ± 0.0005
Fraction of hadron background	0.0146 ± 0.0007
α_s^Z	0.1243 ± 0.0004
α_s^W	0.1263 ± 0.0003
k_T^{intr}	$1.57 \pm 0.14 \text{ GeV}$
A_3 scaling	0.975 ± 0.026
m_W	$80362 \pm 23 \text{ MeV}$

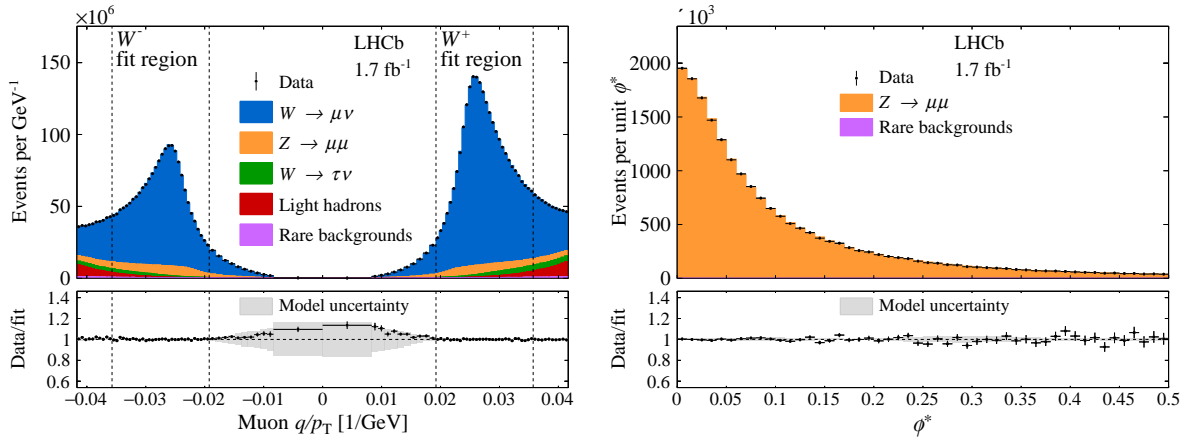


Figure 11: Distributions of (left) q/p_T and (right) ϕ^* compared to the model after the m_W fit.

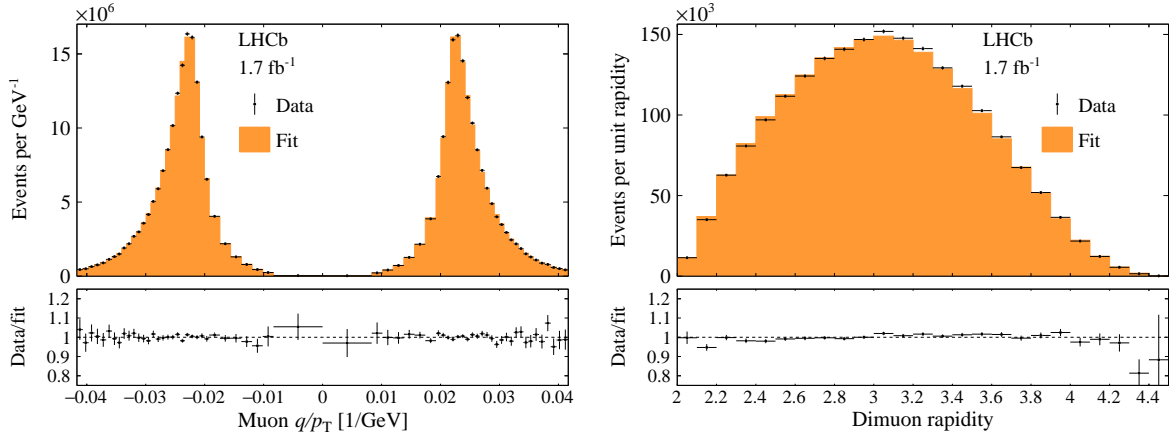


Figure 12: Projections of the (left) q/p_T and (right) rapidity distributions for the Z boson selection. A final state muon is only included in the q/p_T distribution if it satisfies the W boson selection requirements.

Table 5: Uncertainties for the NNPDF3.1, CT18 and MSHT20 sets. The contributions from the PDF uncertainty with fixed α_s and from the α_s variation are quoted separately as is their sum in quadrature, which defines the total uncertainty for each PDF set.

Set	$\sigma_{\text{PDF,base}}$ [MeV]	$\sigma_{\text{PDF},\alpha_s}$ [MeV]	σ_{PDF} [MeV]
NNPDF3.1	8.3	2.4	8.6
CT18	11.5	1.4	11.6
MSHT20	6.5	2.1	6.8

9 Systematic uncertainties and cross-checks

Table 5 lists the PDF uncertainties evaluated for fits based on the NNPDF3.1, CT18 and MSHT20 PDF sets. The m_W values agree within an envelope of 12 MeV, which supports the choice to report an arithmetic average of the three. With respect to the central value obtained with the NNPDF31 PDFs, the m_W values obtained with the CT18 and MSHT20 PDF sets differ by -12 MeV and -11 MeV, respectively. The uncertainties are evaluated according to the specific methods for the three groups. The NNPDF3.1 uncertainty is evaluated as the RMS of m_W values according to 100 replicas, whereas the other two sets use fixed numbers of eigenvectors. The CT18 uncertainty is corrected from 90% confidence level (CL) to 68% CL to be consistent with all other uncertainties in this analysis. For each PDF set, the uncertainty from the replica variations is added in quadrature to the uncertainty from variations in the α_s used in the PDF fits. Values of $0.116 < \alpha_s < 0.120$ are considered, and the uncertainty in m_W is taken as half of the absolute difference between the corresponding shifts in m_W [60].⁶ The PDF uncertainty on the arithmetic average of the three results is taken as the arithmetic average of the three uncertainties, in accordance with the assumption that the uncertainties are fully correlated.

Table 6 lists each contribution to the systematic uncertainty in the final result, after averaging results based on the three PDF sets. The systematic uncertainty is split into three orthogonal components that are combined in quadrature. The uncertainty due to the description of the parton distribution functions is 9 MeV. The remaining theory uncertainty in the modelling of W and Z boson production is 17 MeV, as described in Sect. 7, with the largest contribution arising from variations of the transverse momentum model. The experimental uncertainty is 10 MeV, with the different contributions discussed in Sects. 4, 5, and 6.

Independently of the systematic uncertainty evaluation, several cross-checks of the measurement are performed.

- **Consistency of orthogonal subsets:** The data and simulation are split into orthogonal subsets by magnet polarity, the product of the muon charge and polarity, and the ϕ and η of the muon in the W boson selection. These results are reported in Table 7. Considering the statistical uncertainties only, all differences are within, or just outside, two standard deviations, which was predefined as a criterion for this test.
- **Fit range:** The minimum and maximum p_T of the fit range in the q/p_T distribution

⁶The variations in α_s are larger than the ± 0.0015 variations recommended in Ref. [60] but this choice avoids further *ad hoc* scaling.

Table 6: Contributions to the systematic uncertainty in m_W . Negligible contributions below 1 MeV are not listed.

Source	Size [MeV]
Parton distribution functions	9
Theory (excl. PDFs) total	17
Transverse momentum model	11
Angular coefficients	10
QED FSR model	7
Additional electroweak corrections	5
Experimental total	10
Momentum scale and resolution modelling	7
Muon ID, trigger and tracking efficiency	6
Isolation efficiency	4
QCD background	2
Statistical	23
Total	32

are varied around their default values of 28 GeV and 52 GeV, respectively. The results are reported in Table 8. Considering the variations in the statistical uncertainties in m_W this test shows that the fit results are stable with respect to variations in the fit range.

- Fit model freedom:** The choice of parameters that are determined in the fit is varied and the results are reported in Table 9. The default fit determines one α_s parameter for the Z processes and a second that is shared between W^+ and W^- processes. With three α_s parameters there is only a small change in m_W and the fit quality. The default fit determines a single floating k_T^{intr} parameter that is shared among all three processes. Neither the m_W value nor the χ^2 are strongly affected by allowing two (with one shared between the W^+ and W^- processes) or three k_T^{intr} parameters to vary freely. If the A_3 scaling factor is fixed to unity the value of m_W shifts by 7 MeV and the χ^2 increases by a few units. In summary the m_W fit seems to be rather insensitive to all of these variations, except that the data strongly prefer independent POWHEGPYTHIA tunes for the W and Z boson production processes.
- Use of NNLO PDF sets:** The PDF set used for the analysis is varied from NNPDF31_nlo_as_0118 to NNPDF31_nnlo_as_0118. The shift in m_W is 1 MeV.
- Separate m_W values for W^+ and W^- bosons:** an additional parameter is included in the fit, allowing for separate values of m_W for W^+ and W^- bosons. This mass difference is found to be consistent with zero within one standard deviation.
- W -like measurement of the Z boson mass:** the same methods are applied to the Z boson sample alone, to perform a W -like measurement of the Z boson mass. The values measured with positive and negatively charged muons agree within one standard deviation and their average is consistent with the PDG average [7] within one standard deviation.

Table 7: Fit results where the data and simulation samples are split into two orthogonal subsets. For a given split, the first row is defined as the reference with respect to which the difference in m_W , denoted by δm_W , is defined. The uncertainties quoted on δm_W are statistical.

Subset	$\chi_{\text{tot}}^2/\text{ndf}$	δm_W [MeV]
Polarity = -1	92.5/102	-
Polarity = +1	97.3/102	-57.5 ± 45.4
$\eta > 3.3$	115.4/102	-
$\eta < 3.3$	85.9/102	$+56.9 \pm 45.5$
Polarity $\times q = +1$	95.9/102	-
Polarity $\times q = -1$	98.2/102	$+16.1 \pm 45.4$
$ \phi > \pi/2$	98.8/102	-
$ \phi < \pi/2$	115.0/102	$+66.7 \pm 45.5$
$\phi < 0$	91.8/102	-
$\phi > 0$	103.0/102	-100.5 ± 45.3

Table 8: Fit results with variations in the fit range around the default $p_T^{\text{min}} = 28$ GeV and $p_T^{\text{min}} = 52$ GeV. The second column lists the χ^2 values, the third column lists the shifts in m_W with respect to the default fit and the third column lists the statistical uncertainties in m_W .

Change to fit range	$\chi_{\text{tot}}^2/\text{ndf}$	δm_W [MeV]	$\sigma(m_W)$ [MeV]
$p_T^{\text{min}} = 24$ GeV	96.5/102	+6.8	19.7
$p_T^{\text{min}} = 26$ GeV	97.7/102	+9.6	20.9
$p_T^{\text{min}} = 30$ GeV	102.7/102	+3.0	25.7
$p_T^{\text{min}} = 32$ GeV	84.9/102	-21.6	30.8
$p_T^{\text{max}} = 48$ GeV	105.3/102	-3.8	23.2
$p_T^{\text{max}} = 50$ GeV	103.0/102	-2.1	23.0
$p_T^{\text{max}} = 54$ GeV	96.3/102	-8.6	22.6
$p_T^{\text{max}} = 56$ GeV	103.7/102	-14.3	22.4

Table 9: Fit results with variations in which physics parameters are varying freely.

Configuration change	$\chi_{\text{tot}}^2/\text{ndf}$	δm_W [MeV]	$\sigma(m_W)$ [MeV]
2 \rightarrow 3 α_s parameters	103.4/101	-6.0	± 23.1
2 \rightarrow 1 α_s and 1 \rightarrow 2 k_T^{intr} parameters	116.1/102	+13.9	± 22.4
1 \rightarrow 2 k_T^{intr} parameters	104.0/101	+0.4	± 22.7
1 \rightarrow 3 k_T^{intr} parameters	102.8/100	-2.7	± 22.9
No A_3 scaling	106.0/103	+4.4	± 22.2
Varying QCD background asymmetry	103.8/101	-0.7	± 22.7

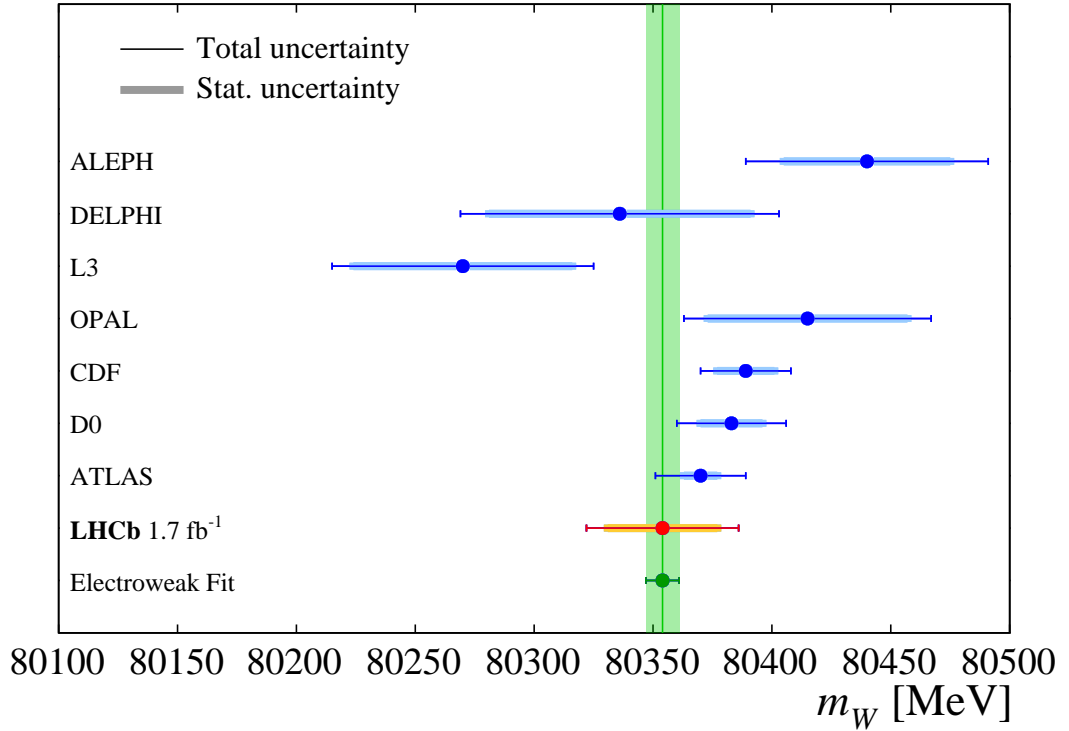


Figure 13: Measured value of m_W compared to those from the ALEPH [61], DELPHI [62], L3 [63], OPAL [64], CDF [10], D0 [11] and ATLAS [12] experiments. The current prediction of m_W from the global electroweak fit is also included.

10 Summary and Conclusion

This paper reports the first measurement of m_W with the LHCb experiment. A data sample of pp collisions at $\sqrt{s} = 13$ TeV corresponding to an integrated luminosity of 1.7 fb^{-1} is analysed. The measurement is based on the shape of the p_T distribution of muons from W boson decays. A simultaneous fit of the q/p_T distribution of W boson decay candidates and of the ϕ^* distribution of Z boson decay candidates is verified to reliably determine m_W . This method has reduced sensitivity to the uncertainties in modelling the W boson transverse momentum distribution compared to previous determinations of m_W at hadron colliders. The following results are obtained

$$\begin{aligned}
 m_W &= 80362 \pm 23_{\text{stat}} \pm 10_{\text{exp}} \pm 17_{\text{theory}} \pm 9_{\text{PDF}} \text{ MeV}, \\
 m_W &= 80350 \pm 23_{\text{stat}} \pm 10_{\text{exp}} \pm 17_{\text{theory}} \pm 12_{\text{PDF}} \text{ MeV}, \\
 m_W &= 80351 \pm 23_{\text{stat}} \pm 10_{\text{exp}} \pm 17_{\text{theory}} \pm 7_{\text{PDF}} \text{ MeV},
 \end{aligned}$$

with the NNPDF3.1, CT18 and MSHT20 PDF sets, respectively. The first uncertainty is statistical, the second is due to experimental systematic uncertainties, and the third and fourth are due to uncertainties in the theoretical modelling and the description of the PDFs, respectively. Treating the three PDF sets equally results in the following arithmetic average

$$m_W = 80354 \pm 23_{\text{stat}} \pm 10_{\text{exp}} \pm 17_{\text{theory}} \pm 9_{\text{PDF}} \text{ MeV}.$$

This result agrees with the current PDG average of direct measurements [7] and the indirect prediction from the global EW fit [6], and is compared to previous measurements in Fig. 13. This measurement also serves as a first proof-of-principle of a measurement of m_W with the LHCb experiment. In Ref. [65] it was demonstrated that the PDF uncertainty in a measurement of m_W by LHCb can be strongly reduced by using *in situ* constraints and by fitting the doubly differential distribution of p_T and η , similar to the measurement by the CMS Collaboration [66], instead of the singly differential p_T distribution. An approximately three times larger data sample is already available for analysis but particular attention should be paid to reducing the dominant source of systematic uncertainty, which is the modelling of W boson production.

Acknowledgements

We express our gratitude to our colleagues in the CERN accelerator departments for the excellent performance of the LHC. We thank the technical and administrative staff at the LHCb institutes. We acknowledge support from CERN and from the national agencies: CAPES, CNPq, FAPERJ and FINEP (Brazil); MOST and NSFC (China); CNRS/IN2P3 (France); BMBF, DFG and MPG (Germany); INFN (Italy); NWO (Netherlands); MNiSW and NCN (Poland); MEN/IFA (Romania); MSHE (Russia); MICINN (Spain); SNSF and SER (Switzerland); NASU (Ukraine); STFC (United Kingdom); DOE NP and NSF (USA). We acknowledge the computing resources that are provided by CERN, IN2P3 (France), KIT and DESY (Germany), INFN (Italy), SURF (Netherlands), PIC (Spain), GridPP (United Kingdom), RRCKI and Yandex LLC (Russia), CSCS (Switzerland), IFIN-HH (Romania), CBPF (Brazil), PL-GRID (Poland) and NERSC (USA). We are indebted to the communities behind the multiple open-source software packages on which we depend. Individual groups or members have received support from ARC and ARDC (Australia); AvH Foundation (Germany); EPLANET, Marie Skłodowska-Curie Actions and ERC (European Union); A*MIDEX, ANR, IPhU and Labex P2IO, and Région Auvergne-Rhône-Alpes (France); Key Research Program of Frontier Sciences of CAS, CAS PIFI, CAS CCEPP, Fundamental Research Funds for the Central Universities, and Sci. & Tech. Program of Guangzhou (China); RFBR, RSF and Yandex LLC (Russia); GVA, XuntaGal and GENCAT (Spain); the Leverhulme Trust, the Royal Society and UKRI (United Kingdom).

References

- [1] S. L. Glashow, *Partial Symmetries of Weak Interactions*, Nucl. Phys. **22** (1961) 579.
- [2] S. Weinberg, *A model of leptons*, Phys. Rev. Lett. **19** (1967) 1264.
- [3] A. Salam and J. C. Ward, *Electromagnetic and weak interactions*, Physics Letters **13** (1964) 168.
- [4] M. Awramik, M. Czakon, A. Freitas, and G. Weiglein, *Precise prediction for the W boson mass in the standard model*, Phys. Rev. **D69** (2004) 053006, [arXiv:hep-ph/0311148](https://arxiv.org/abs/hep-ph/0311148).

- [5] A. Sirlin, *Radiative corrections in the $SU(2)_L \times U(1)$ theory: A simple renormalization framework*, Phys. Rev. **D22** (1980) 971.
- [6] J. Haller *et al.*, *Update of the global electroweak fit and constraints on two-Higgs-doublet models*, Eur. Phys. J. **C78** (2018) 675, [arXiv:1803.01853](#).
- [7] Particle Data Group, P. A. Zyla *et al.*, *Review of particle physics*, Prog. Theor. Exp. Phys. **2020** (2020) 083C01.
- [8] ALEPH, DELPHI, L3, OPAL, LEP Electroweak collaboration, S. Schael *et al.*, *Electroweak Measurements in Electron-Positron Collisions at W-Boson-Pair Energies at LEP*, Phys. Rept. **532** (2013) 119, [arXiv:1302.3415](#).
- [9] CDF, D0 collaboration, T. A. Aaltonen *et al.*, *Combination of CDF and D0 W-boson mass measurements*, Phys. Rev. D **88** (2013) 052018, [arXiv:1307.7627](#).
- [10] CDF collaboration, T. Aaltonen *et al.*, *Precise measurement of the W-boson mass with the CDF II detector*, Phys. Rev. Lett. **108** (2012) 151803, [arXiv:1203.0275](#).
- [11] D0 collaboration, V. M. Abazov *et al.*, *Measurement of the W Boson mass with the D0 Detector*, Phys. Rev. Lett. **108** (2012) 151804, [arXiv:1203.0293](#).
- [12] ATLAS collaboration, M. Aaboud *et al.*, *Measurement of the W-boson mass in pp collisions at $\sqrt{s} = 7$ TeV with the ATLAS detector*, Eur. Phys. J. **C78** (2018) 110, Erratum *ibid.* **C78** (2018) 898, [arXiv:1701.07240](#).
- [13] G. Bozzi *et al.*, *Prospects for improving the LHC W boson mass measurement with forward muons*, Eur. Phys. J. **C75** (2015) 601, [arXiv:1508.06954](#).
- [14] G. Aad *et al.*, *Measurement of the transverse momentum distribution of W bosons in pp collisions $\sqrt{s}=7$ TeV with the ATLAS detector*, Physical Review **D85** (2012) , [arXiv:1108.6308](#).
- [15] CMS collaboration, V. Khachatryan *et al.*, *Measurement of the transverse momentum spectra of weak vector bosons produced in proton-proton collisions at $\sqrt{s} = 8$ TeV*, JHEP **02** (2017) 096, [arXiv:1606.05864](#).
- [16] A. Banfi *et al.*, *Optimisation of variables for studying dilepton transverse momentum distributions at hadron colliders*, Eur. Phys. J. C **71** (2011) 1600, [arXiv:1009.1580](#).
- [17] T. Sjöstrand *et al.*, *An introduction to PYTHIA 8.2*, Comput. Phys. Commun. **191** (2015) 159, [arXiv:1410.3012](#).
- [18] P. Skands, S. Carrazza, and J. Rojo, *Tuning PYTHIA 8.1: the Monash 2013 Tune*, Eur. Phys. J. **C74** (2014) 3024, [arXiv:1404.5630](#).
- [19] O. Lupton and M. Vesterinen, *Simultaneously determining the W^\pm boson mass and parton shower model parameters*, [arXiv:1907.09958](#).
- [20] J. C. Collins and D. E. Soper, *Angular distribution of dileptons in high-energy hadron collisions*, Phys. Rev. **D16** (1977) 2219.

- [21] LHCb collaboration, A. A. Alves Jr. *et al.*, *The LHCb detector at the LHC*, JINST **3** (2008) S08005.
- [22] LHCb collaboration, R. Aaij *et al.*, *LHCb detector performance*, Int. J. Mod. Phys. **A30** (2015) 1530022, arXiv:1412.6352.
- [23] R. Aaij *et al.*, *Performance of the LHCb Vertex Locator*, JINST **9** (2014) P09007, arXiv:1405.7808.
- [24] P. d'Argent *et al.*, *Improved performance of the LHCb Outer Tracker in LHC Run 2*, JINST **12** (2017) P11016, arXiv:1708.00819.
- [25] M. Adinolfi *et al.*, *Performance of the LHCb RICH detector at the LHC*, Eur. Phys. J. **C73** (2013) 2431, arXiv:1211.6759.
- [26] A. A. Alves Jr. *et al.*, *Performance of the LHCb muon system*, JINST **8** (2013) P02022, arXiv:1211.1346.
- [27] R. Aaij *et al.*, *The LHCb trigger and its performance in 2011*, JINST **8** (2013) P04022, arXiv:1211.3055.
- [28] R. Aaij *et al.*, *Performance of the LHCb trigger and full real-time reconstruction in Run 2 of the LHC*, JINST **14** (2019) P04013, arXiv:1812.10790.
- [29] W. D. Hulsbergen, *The global covariance matrix of tracks fitted with a Kalman filter and an application in detector alignment*, Nucl. Instr. Meth. **600** (2009) 471–477, arXiv:0810.2241.
- [30] J. Amoraal *et al.*, *Application of vertex and mass constraints in track-based alignment*, Nucl. Instrum. Meth. **712** (2013) 48–55, arXiv:1207.4756.
- [31] I. Belyaev *et al.*, *Handling of the generation of primary events in Gauss, the LHCb simulation framework*, J. Phys. Conf. Ser. **331** (2011) 032047.
- [32] Geant4 collaboration, J. Allison *et al.*, *Geant4 developments and applications*, IEEE Trans. Nucl. Sci. **53** (2006) 270; Geant4 collaboration, S. Agostinelli *et al.*, *Geant4: A simulation toolkit*, Nucl. Instrum. Meth. **A506** (2003) 250.
- [33] M. Clemencic *et al.*, *The LHCb simulation application, Gauss: Design, evolution and experience*, J. Phys. Conf. Ser. **331** (2011) 032023.
- [34] LHCb collaboration, R. Aaij *et al.*, *Study of forward Z +jet production in pp collisions at $\sqrt{s} = 7$ TeV*, JHEP **01** (2014) 033, arXiv:1310.8197.
- [35] W. Barter, M. Pili, and M. Vesterinen, *A simple method to determine charge-dependent curvature biases in track reconstruction in hadron collider experiments*, Eur. Phys. J. **C81** (2021) 251, arXiv:2101.05675.
- [36] T. Skwarnicki, *A study of the radiative cascade transitions between the Upsilon-prime and Upsilon resonances*, PhD thesis, Institute of Nuclear Physics, Krakow, 1986, DESY-F31-86-02.

- [37] LHCb collaboration, R. Aaij *et al.*, *Measurement of the forward Z boson production cross-section in pp collisions at $\sqrt{s}=13$ TeV*, JHEP **09** (2016) 136, [arXiv:1607.06495](#).
- [38] LHCb collaboration, R. Aaij *et al.*, *Production of J/ψ and Υ mesons in pp collisions at $\sqrt{s}=8$ TeV*, JHEP **06** (2013) 064, [arXiv:1304.6977](#).
- [39] LHCb collaboration, R. Aaij *et al.*, *Measurement of the track reconstruction efficiency at LHCb*, JINST **10** (2015) P02007, [arXiv:1408.1251](#).
- [40] R. Hagedorn, *Multiplicities, p_T Distributions and the Expected Hadron \rightarrow Quark - Gluon Phase Transition*, Riv. Nuovo Cim. **6N10** (1983) 1.
- [41] L. Barze *et al.*, *Implementation of electroweak corrections in the POWHEG BOX: single W production*, JHEP **04** (2012) 037, [arXiv:1202.0465](#).
- [42] L. Barze *et al.*, *Neutral current Drell-Yan with combined QCD and electroweak corrections in the POWHEG BOX*, Eur. Phys. J. **C73** (2013) 2474, [arXiv:1302.4606](#).
- [43] C. M. Carloni Calame *et al.*, *Precision Measurement of the W-Boson mass: Theoretical Contributions and Uncertainties*, Phys. Rev. **D96** (2017) 093005, [arXiv:1612.02841](#).
- [44] NNPDF collaboration, R. D. Ball *et al.*, *Parton distributions with QED corrections*, Nucl. Phys. **B877** (2013) 290, [arXiv:1308.0598](#).
- [45] A. Buckley *et al.*, *LHAPDF6: parton density access in the LHC precision era*, Eur. Phys. J. **C75** (2015) 132, [arXiv:1412.7420](#).
- [46] NNPDF collaboration, R. D. Ball *et al.*, *Parton distributions from high-precision collider data*, Eur. Phys. J. **C77** (2017) 663, [arXiv:1706.00428](#).
- [47] H.-L. Lai *et al.*, *Parton Distributions for Event Generators*, JHEP **04** (2010) 035, [arXiv:0910.4183](#).
- [48] S. Alioli, P. Nason, C. Oleari, and E. Re, *NLO vector-boson production matched with shower in POWHEG*, JHEP **07** (2008) 060, [arXiv:0805.4802](#).
- [49] J. Bellm *et al.*, *Herwig 7.0/Herwig++ 3.0 release note*, Eur. Phys. J. **C76** (2016) 196, [arXiv:1512.01178](#).
- [50] S. Camarda *et al.*, *DYTurbo: fast predictions for Drell-Yan processes*, Eur. Phys. J. **C80** (2020) 251, Erratum *ibid.* **C80** (2020) 440, [arXiv:1910.07049](#).
- [51] ATLAS collaboration, G. Aad *et al.*, *Measurement of the angular coefficients in Z-boson events using electron and muon pairs from data taken at $\sqrt{s}=8$ TeV with the ATLAS detector*, JHEP **08** (2016) 159, [arXiv:1606.00689](#).
- [52] S. Catani *et al.*, *Vector boson production at hadron colliders: a fully exclusive QCD calculation at NNLO*, Phys. Rev. Lett. **103** (2009) 082001, [arXiv:0903.2120](#).
- [53] R. Gauld *et al.*, *Precise predictions for the angular coefficients in Z-boson production at the LHC*, JHEP **11** (2017) 003, [arXiv:1708.00008](#).

- [54] NNPDF collaboration, R. D. Ball *et al.*, *Precision determination of the strong coupling constant within a global PDF analysis*, Eur. Phys. J. **C78** (2018) 408, [arXiv:1802.03398](#).
- [55] T.-J. Hou *et al.*, *New CTEQ global analysis of quantum chromodynamics with high-precision data from the LHC*, Phys. Rev. **D103** (2021) 014013, [arXiv:1912.10053](#).
- [56] S. Bailey *et al.*, *Parton distributions from LHC, HERA, Tevatron and fixed target data: MSHT20 PDFs*, Eur. Phys. J. **C81** (2021) 341, [arXiv:2012.04684](#).
- [57] N. Davidson, T. Przedzinski, and Z. Was, *PHOTOS interface in C++: Technical and physics documentation*, Comp. Phys. Comm. **199** (2016) 86, [arXiv:1011.0937](#).
- [58] R. J. Barlow and C. Beeston, *Fitting using finite Monte Carlo samples*, Comput. Phys. Commun. **77** (1993) 219.
- [59] LHCb collaboration, R. Aaij *et al.*, *Measurement of forward W and Z boson production in pp collisions at $\sqrt{s} = 8$ TeV*, JHEP **01** (2016) 155, [arXiv:1511.08039](#).
- [60] J. Butterworth *et al.*, *PDF4LHC recommendations for LHC Run II*, J. Phys. **G43** (2016) 023001, [arXiv:1510.03865](#).
- [61] ALEPH collaboration, S. Schael *et al.*, *Measurement of the W boson mass and width in e^+e^- collisions at LEP*, Eur. Phys. J. C **47** (2006) 309, [arXiv:hep-ex/0605011](#).
- [62] DELPHI collaboration, J. Abdallah *et al.*, *Measurement of the mass and width of the W boson in e^+e^- collisions at $\sqrt{s} = 161$ -GeV - 209-GeV*, Eur. Phys. J. C **55** (2008) 1, [arXiv:0803.2534](#).
- [63] L3 collaboration, P. Achard *et al.*, *Measurement of the mass and the width of the W boson at LEP*, Eur. Phys. J. C **45** (2006) 569, [arXiv:hep-ex/0511049](#).
- [64] OPAL collaboration, G. Abbiendi *et al.*, *Measurement of the mass and width of the W boson*, Eur. Phys. J. C **45** (2006) 307, [arXiv:hep-ex/0508060](#).
- [65] S. Farry *et al.*, *Understanding and constraining the PDF uncertainties in a W boson mass measurement with forward muons at the LHC*, Eur. Phys. J. **C79** (2019) 497, [arXiv:1902.04323](#).
- [66] CMS collaboration, A. M. Sirunyan *et al.*, *Measurements of the W boson rapidity, helicity, double-differential cross sections, and charge asymmetry in pp collisions at $\sqrt{s} = 13$ TeV*, Phys. Rev. D **102** (2020) 092012, [arXiv:2008.04174](#).

LHCb collaboration

R. Aaij³², A.S.W. Abdelmotteleb⁵⁶, C. Abellán Beteta⁵⁰, T. Ackernley⁶⁰, B. Adeva⁴⁶, M. Adinolfi⁵⁴, H. Afsharnia⁹, C. Agapopoulou¹³, C.A. Aidala⁸⁶, S. Aiola²⁵, Z. Ajaltouni⁹, S. Akar⁶⁵, J. Albrecht¹⁵, F. Alessio⁴⁸, M. Alexander⁵⁹, A. Alfonso Alberio⁴⁵, Z. Aliouche⁶², G. Alkhazov³⁸, P. Alvarez Cartelle⁵⁵, S. Amato², J.L. Amey⁵⁴, Y. Amhis¹¹, L. An⁴⁸, L. Anderlini²², A. Andreianov³⁸, M. Andreotti²¹, F. Archilli¹⁷, A. Artamonov⁴⁴, M. Artuso⁶⁸, K. Arzymatov⁴², E. Aslanides¹⁰, M. Atzeni⁵⁰, B. Audurier¹², S. Bachmann¹⁷, M. Bachmayer⁴⁹, J.J. Back⁵⁶, P. Baladron Rodriguez⁴⁶, V. Balagura¹², W. Baldini²¹, J. Baptista Leite¹, M. Barbetti²², R.J. Barlow⁶², S. Barsuk¹¹, W. Barter⁶¹, M. Bartolini²⁴, F. Baryshnikov⁸³, J.M. Basels¹⁴, S. Bashir³⁴, G. Bassi²⁹, B. Batsukh⁶⁸, A. Battig¹⁵, A. Bay⁴⁹, A. Beck⁵⁶, M. Becker¹⁵, F. Bedeschi²⁹, I. Bediaga¹, A. Beiter⁶⁸, V. Belavin⁴², S. Belin²⁷, V. Bellee⁵⁰, K. Belous⁴⁴, I. Belov⁴⁰, I. Belyaev⁴¹, G. Bencivenni²³, E. Ben-Haim¹³, A. Berezhnoy⁴⁰, R. Bernet⁵⁰, D. Berninghoff¹⁷, H.C. Bernstein⁶⁸, C. Bertella⁴⁸, A. Bertolin²⁸, C. Betancourt⁵⁰, F. Betti⁴⁸, I.A. Bezshyiko⁵⁰, S. Bhasin⁵⁴, J. Bhom³⁵, L. Bian⁷³, M.S. Bieker¹⁵, S. Bifani⁵³, P. Billoir¹³, M. Birch⁶¹, F.C.R. Bishop⁵⁵, A. Bitadze⁶², A. Bizzeti^{22,k}, M. Bjørn⁶³, M.P. Blago⁴⁸, T. Blake⁵⁶, F. Blanc⁴⁹, S. Blusk⁶⁸, D. Bobulska⁵⁹, J.A. Boelhauve¹⁵, O. Boente Garcia⁴⁶, T. Boettcher⁶⁵, A. Boldyrev⁸², A. Bondar⁴³, N. Bondar^{38,48}, S. Borghi⁶², M. Borisyak⁴², M. Borsato¹⁷, J.T. Borsuk³⁵, S.A. Bouchiba⁴⁹, T.J.V. Bowcock⁶⁰, A. Boyer⁴⁸, C. Bozzi²¹, M.J. Bradley⁶¹, S. Braun⁶⁶, A. Brea Rodriguez⁴⁶, M. Brodski⁴⁸, J. Brodzicka³⁵, A. Brossa Gonzalo⁵⁶, D. Brundu²⁷, A. Buonaura⁵⁰, L. Buonincontri²⁸, A.T. Burke⁶², C. Burr⁴⁸, A. Bursche⁷², A. Butkevich³⁹, J.S. Butter³², J. Buytaert⁴⁸, W. Byczynski⁴⁸, S. Cadeddu²⁷, H. Cai⁷³, R. Calabrese^{21,f}, L. Calefice^{15,13}, L. Calero Diaz²³, S. Cali²³, R. Calladine⁵³, M. Calvi^{26,j}, M. Calvo Gomez⁸⁵, P. Camargo Magalhaes⁵⁴, P. Campana²³, A.F. Campoverde Quezada⁶, S. Capelli^{26,j}, L. Capriotti^{20,d}, A. Carbone^{20,d}, G. Carboni³¹, R. Cardinale²⁴, A. Cardini²⁷, I. Carli⁴, P. Carniti^{26,j}, L. Carus¹⁴, K. Carvalho Akiba³², A. Casais Vidal⁴⁶, G. Casse⁶⁰, M. Cattaneo⁴⁸, G. Cavallero⁴⁸, S. Celani⁴⁹, J. Cerasoli¹⁰, D. Cervenkov⁶³, A.J. Chadwick⁶⁰, M.G. Chapman⁵⁴, M. Charles¹³, Ph. Charpentier⁴⁸, G. Chatzikonstantinidis⁵³, C.A. Chavez Barajas⁶⁰, M. Chefdeville⁸, C. Chen³, S. Chen⁴, A. Chernov³⁵, V. Chobanova⁴⁶, S. Cholak⁴⁹, M. Chruszcz³⁵, A. Chubykin³⁸, V. Chulikov³⁸, P. Ciambri²³, M.F. Cicala⁵⁶, X. Cid Vidal⁴⁶, G. Ciezarek⁴⁸, P.E.L. Clarke⁵⁸, M. Clemencic⁴⁸, H.V. Cliff⁵⁵, J. Closier⁴⁸, J.L. Cobbledick⁶², V. Coco⁴⁸, J.A.B. Coelho¹¹, J. Cogan¹⁰, E. Cogneras⁹, L. Cojocariu³⁷, P. Collins⁴⁸, T. Colombo⁴⁸, L. Congedo^{19,c}, A. Contu²⁷, N. Cooke⁵³, G. Coombs⁵⁹, I. Corredoira⁴⁶, G. Corti⁴⁸, C.M. Costa Sobral⁵⁶, B. Couturier⁴⁸, D.C. Craik⁶⁴, J. Crkovská⁶⁷, M. Cruz Torres¹, R. Currie⁵⁸, C.L. Da Silva⁶⁷, S. Dadabaev⁸³, L. Dai⁷¹, E. Dall'Occo¹⁵, J. Dalseno⁴⁶, C. D'Ambrosio⁴⁸, A. Danilina⁴¹, P. d'Argent⁴⁸, J.E. Davies⁶², A. Davis⁶², O. De Aguiar Francisco⁶², K. De Bruyn⁷⁹, S. De Capua⁶², M. De Cian⁴⁹, J.M. De Miranda¹, L. De Paula², M. De Serio^{19,c}, D. De Simone⁵⁰, P. De Simone²³, J.A. de Vries⁸⁰, C.T. Dean⁶⁷, D. Decamp⁸, V. Dedu¹⁰, L. Del Buono¹³, B. Delaney⁵⁵, H.-P. Dembinski¹⁵, A. Dendek³⁴, V. Denysenko⁵⁰, D. Derkach⁸², O. Deschamps⁹, F. Desse¹¹, F. Dettori^{27,e}, B. Dey⁷⁷, A. Di Cicco²³, P. Di Nezza²³, S. Didenko⁸³, L. Dieste Maronas⁴⁶, H. Dijkstra⁴⁸, V. Dobishuk⁵², C. Dong³, A.M. Donohoe¹⁸, F. Dordei²⁷, A.C. dos Reis¹, L. Douglas⁵⁹, A. Dovbnya⁵¹, A.G. Downes⁸, M.W. Dudek³⁵, L. Dufour⁴⁸, V. Duk⁷⁸, P. Durante⁴⁸, J.M. Durham⁶⁷, D. Dutta⁶², A. Dziurda³⁵, A. Dzyuba³⁸, S. Easo⁵⁷, U. Egede⁶⁹, V. Egorychev⁴¹, S. Eidelman^{43,v}, S. Eisenhardt⁵⁸, S. Ek-In⁴⁹, L. Eklund^{59,w}, S. Ely⁶⁸, A. Ene³⁷, E. Epple⁶⁷, S. Escher¹⁴, J. Eschle⁵⁰, S. Esen¹³, T. Evans⁴⁸, A. Falabella²⁰, J. Fan³, Y. Fan⁶, B. Fang⁷³, S. Farry⁶⁰, D. Fazzini^{26,j}, M. Féo⁴⁸, A. Fernandez Prieto⁴⁶, J.M. Fernandez-tenllado Arribas⁴⁵, A.D. Fernez⁶⁶, F. Ferrari^{20,d}, L. Ferreira Lopes⁴⁹, F. Ferreira Rodrigues², S. Ferreres Sole³², M. Ferrillo⁵⁰, M. Ferro-Luzzi⁴⁸, S. Filippov³⁹, R.A. Fini¹⁹, M. Fiorini^{21,f}, M. Firlej³⁴, K.M. Fischer⁶³, D.S. Fitzgerald⁸⁶, C. Fitzpatrick⁶²,

T. Fiutowski³⁴, A. Fkiaras⁴⁸, F. Fleuret¹², M. Fontana¹³, F. Fontanelli^{24,h}, R. Forty⁴⁸,
 D. Foulds-Holt⁵⁵, V. Franco Lima⁶⁰, M. Franco Sevilla⁶⁶, M. Frank⁴⁸, E. Franzoso²¹, G. Frau¹⁷,
 C. Frei⁴⁸, D.A. Friday⁵⁹, J. Fu²⁵, Q. Fuehring¹⁵, E. Gabriel³², A. Gallas Torreira⁴⁶, D. Galli^{20,d},
 S. Gambetta^{58,48}, Y. Gan³, M. Gandelman², P. Gandini²⁵, Y. Gao⁵, M. Garau²⁷,
 L.M. Garcia Martin⁵⁶, P. Garcia Moreno⁴⁵, J. García Pardiñas^{26,j}, B. Garcia Plana⁴⁶,
 F.A. Garcia Rosales¹², L. Garrido⁴⁵, C. Gaspar⁴⁸, R.E. Geertsema³², D. Gerick¹⁷,
 L.L. Gerken¹⁵, E. Gersabeck⁶², M. Gersabeck⁶², T. Gershon⁵⁶, D. Gerstel¹⁰, Ph. Ghez⁸,
 L. Giambastiani²⁸, V. Gibson⁵⁵, H.K. Giemza³⁶, A.L. Gilman⁶³, M. Giovannetti^{23,p},
 A. Gioventù⁴⁶, P. Gironella Gironell⁴⁵, L. Giubega³⁷, C. Giugliano^{21,f,48}, K. Gizdov⁵⁸,
 E.L. Gkougkousis⁴⁸, V.V. Gligorov¹³, C. Göbel⁷⁰, E. Golobardes⁸⁵, D. Golubkov⁴¹,
 A. Golutvin^{61,83}, A. Gomes^{1,a}, S. Gomez Fernandez⁴⁵, F. Goncalves Abrantes⁶³, M. Goncerz³⁵,
 G. Gong³, P. Gorbounov⁴¹, I.V. Gorelov⁴⁰, C. Gotti²⁶, E. Govorkova⁴⁸, J.P. Grabowski¹⁷,
 T. Grammatico¹³, L.A. Granado Cardoso⁴⁸, E. Graugés⁴⁵, E. Graverini⁴⁹, G. Graziani²²,
 A. Grecu³⁷, L.M. Greeven³², N.A. Grieser⁴, L. Grillo⁶², S. Gromov⁸³, B.R. Gruberg Cazon⁶³,
 C. Gu³, M. Guarise²¹, M. Guittiere¹¹, P. A. Günther¹⁷, E. Gushchin³⁹, A. Guth¹⁴, Y. Guz⁴⁴,
 T. Gys⁴⁸, T. Hadavizadeh⁶⁹, G. Haefeli⁴⁹, C. Haen⁴⁸, J. Haimberger⁴⁸, T. Halewood-leagas⁶⁰,
 P.M. Hamilton⁶⁶, J.P. Hammerich⁶⁰, Q. Han⁷, X. Han¹⁷, T.H. Hancock⁶³,
 S. Hansmann-Menzemer¹⁷, N. Harnew⁶³, T. Harrison⁶⁰, C. Hasse⁴⁸, M. Hatch⁴⁸, J. He^{6,b},
 M. Hecker⁶¹, K. Heijhoff³², K. Heinicke¹⁵, A.M. Hennequin⁴⁸, K. Hennessy⁶⁰, L. Henry⁴⁸,
 J. Heuel¹⁴, A. Hicheur², D. Hill⁴⁹, M. Hilton⁶², S.E. Hollitt¹⁵, R. Hou⁷, Y. Hou⁶, J. Hu¹⁷,
 J. Hu⁷², W. Hu⁷, X. Hu³, W. Huang⁶, X. Huang⁷³, W. Hulsbergen³², R.J. Hunter⁵⁶,
 M. Hushchyn⁸², D. Hutchcroft⁶⁰, D. Hynds³², P. Ibis¹⁵, M. Idzik³⁴, D. Ilin³⁸, P. Ilten⁶⁵,
 A. Inglessi³⁸, A. Ishteev⁸³, K. Ivshin³⁸, R. Jacobsson⁴⁸, H. Jage¹⁴, S. Jakobsen⁴⁸, E. Jans³²,
 B.K. Jashal⁴⁷, A. Jawahery⁶⁶, V. Jevtic¹⁵, M. Jezabek³⁵, F. Jiang³, M. John⁶³, D. Johnson⁴⁸,
 C.R. Jones⁵⁵, T.P. Jones⁵⁶, B. Jost⁴⁸, N. Jurik⁴⁸, S.H. Kalavan Kadavath³⁴, S. Kandybei⁵¹,
 Y. Kang³, M. Karacson⁴⁸, M. Karpov⁸², F. Keizer⁴⁸, D.M. Keller⁶⁸, M. Kenzie⁵⁶, T. Ketel³³,
 B. Khanji¹⁵, A. Kharisova⁸⁴, S. Kholodenko⁴⁴, T. Kirn¹⁴, V.S. Kirsebom⁴⁹, O. Kitouni⁶⁴,
 S. Klaver³², N. Kleijne²⁹, K. Klimaszewski³⁶, M.R. Kmiec³⁶, S. Koliiev⁵², A. Kondybayeva⁸³,
 A. Konoplyannikov⁴¹, P. Kopciwicz³⁴, R. Kopečna¹⁷, P. Koppenburg³², M. Korolev⁴⁰,
 I. Kostiuk^{32,52}, O. Kot⁵², S. Kotriakhova^{21,38}, P. Kravchenko³⁸, L. Kravchuk³⁹,
 R.D. Krawczyk⁴⁸, M. Kreps⁵⁶, F. Kress⁶¹, S. Kretzschmar¹⁴, P. Krokovny^{43,v}, W. Krupa³⁴,
 W. Krzemien³⁶, W. Kucewicz^{35,t}, M. Kucharczyk³⁵, V. Kudryavtsev^{43,v}, H.S. Kuindersma^{32,33},
 G.J. Kunde⁶⁷, T. Kvaratskheliya⁴¹, D. Lacarrere⁴⁸, G. Lafferty⁶², A. Lai²⁷, A. Lampis²⁷,
 D. Lancierini⁵⁰, J.J. Lane⁶², R. Lane⁵⁴, G. Lanfranchi²³, C. Langenbruch¹⁴, J. Langer¹⁵,
 O. Lantwin⁸³, T. Latham⁵⁶, F. Lazzari^{29,q}, R. Le Gac¹⁰, S.H. Lee⁸⁶, R. Lefèvre⁹, A. Leflat⁴⁰,
 S. Legotin⁸³, O. Leroy¹⁰, T. Lesiak³⁵, B. Leverington¹⁷, H. Li⁷², P. Li¹⁷, S. Li⁷, Y. Li⁴, Y. Li⁴,
 Z. Li⁶⁸, X. Liang⁶⁸, T. Lin⁶¹, R. Lindner⁴⁸, V. Lisovskyi¹⁵, R. Litvinov²⁷, G. Liu⁷², H. Liu⁶,
 S. Liu⁴, A. Lobo Salvia⁴⁵, A. Loi²⁷, J. Lomba Castro⁴⁶, I. Longstaff⁵⁹, J.H. Lopes²,
 S. Lopez Solino⁴⁶, G.H. Lovell⁵⁵, Y. Lu⁴, C. Lucarelli²², D. Lucchesi^{28,l}, S. Luchuk³⁹,
 M. Lucio Martinez³², V. Lukashenko³², Y. Luo³, A. Lupato⁶², E. Luppi^{21,f}, O. Lupton⁵⁶,
 A. Lusiani^{29,m}, X. Lyu⁶, L. Ma⁴, R. Ma⁶, S. Maccolini^{20,d}, F. Macheferri¹¹, F. Maciuc³⁷,
 V. Macko⁴⁹, P. Mackowiak¹⁵, S. Maddrell-Mander⁵⁴, O. Madejczyk^t, L.R. Madhan Mohan⁵⁴,
 O. Maev³⁸, A. Maevskiy⁸², D. Maisuzenko³⁸, M.W. Majewski^t, J.J. Malczewski³⁵, S. Malde⁶³,
 B. Malecki⁴⁸, A. Malinin⁸¹, T. Maltsev^{43,v}, H. Malygina¹⁷, G. Manca^{27,e}, G. Mancinelli¹⁰,
 D. Manuzzi^{20,d}, D. Marangotto^{25,i}, J. Maratas^{9,s}, J.F. Marchand⁸, U. Marconi²⁰, S. Mariani^{22,g},
 C. Marin Benito⁴⁸, M. Marinangeli⁴⁹, J. Marks¹⁷, A.M. Marshall⁵⁴, P.J. Marshall⁶⁰,
 G. Martelli⁷⁸, G. Martellotti³⁰, L. Martinazzoli^{48,j}, M. Martinelli^{26,j}, D. Martinez Santos⁴⁶,
 F. Martinez Vidal⁴⁷, A. Massafferri¹, M. Materok¹⁴, R. Matev⁴⁸, A. Mathad⁵⁰, Z. Mathe⁴⁸,
 V. Matiunin⁴¹, C. Matteuzzi²⁶, K.R. Mattioli⁸⁶, A. Mauri³², E. Maurice¹², J. Mauricio⁴⁵,
 M. Mazurek⁴⁸, M. McCann⁶¹, L. Mcconnell¹⁸, T.H. Mcgrath⁶², N.T. Mchugh⁵⁹, A. McNab⁶²,

R. McNulty¹⁸, J.V. Mead⁶⁰, B. Meadows⁶⁵, G. Meier¹⁵, N. Meinert⁷⁶, D. Melnychuk³⁶,
 S. Meloni^{26,j}, M. Merk^{32,80}, A. Merli²⁵, L. Meyer Garcia², M. Mikhasenko⁴⁸, D.A. Milanes⁷⁴,
 E. Millard⁵⁶, M. Milovanovic⁴⁸, M.-N. Minard⁸, A. Minotti^{26,j}, L. Minzoni^{21,f}, S.E. Mitchell⁵⁸,
 B. Mitreska⁶², D.S. Mitzel⁴⁸, A. Mödden¹⁵, R.A. Mohammed⁶³, R.D. Moise⁶¹,
 T. Mombächer⁴⁶, I.A. Monroy⁷⁴, S. Monteil⁹, M. Morandin²⁸, G. Morello²³, M.J. Morello^{29,m},
 J. Moron³⁴, A.B. Morris⁷⁵, A.G. Morris⁵⁶, R. Mountain⁶⁸, H. Mu³, F. Muheim^{58,48},
 M. Mulder⁴⁸, D. Müller⁴⁸, K. Müller⁵⁰, C.H. Murphy⁶³, D. Murray⁶², P. Muzzetto^{27,48},
 P. Naik⁵⁴, T. Nakada⁴⁹, R. Nandakumar⁵⁷, T. Nanut⁴⁹, I. Nasteva², M. Needham⁵⁸, I. Neri²¹,
 N. Neri^{25,i}, S. Neubert⁷⁵, N. Neufeld⁴⁸, R. Newcombe⁶¹, T.D. Nguyen⁴⁹, C. Nguyen-Mau^{49,x},
 E.M. Niel¹¹, S. Nieswand¹⁴, N. Nikitin⁴⁰, N.S. Nolte⁶⁴, C. Normand⁸, C. Nunez⁸⁶,
 A. Oblakowska-Mucha³⁴, V. Obraztsov⁴⁴, T. Oeser¹⁴, D.P. O'Hanlon⁵⁴, S. Okamura²¹,
 R. Oldeman^{27,e}, F. Oliva⁵⁸, M.E. Olivares⁶⁸, C.J.G. Onderwater⁷⁹, R.H. O'neil⁵⁸,
 A. Ossowska³⁵, J.M. Otalora Goicochea², T. Ovsianikova⁴¹, P. Owen⁵⁰, A. Oyanguren⁴⁷,
 K.O. Padeken⁷⁵, B. Pagare⁵⁶, P.R. Pais⁴⁸, T. Pajero⁶³, A. Palano¹⁹, M. Palutan²³, Y. Pan⁶²,
 G. Panshin⁸⁴, A. Papanestis⁵⁷, M. Pappagallo^{19,c}, L.L. Pappalardo^{21,f}, C. Pappenheimer⁶⁵,
 W. Parker⁶⁶, C. Parkes⁶², B. Passalacqua²¹, G. Passaleva²², A. Pastore¹⁹, M. Patel⁶¹,
 C. Patrignani^{20,d}, C.J. Pawley⁸⁰, A. Pearce⁴⁸, A. Pellegrino³², M. Pepe Altarelli⁴⁸,
 S. Perazzini²⁰, D. Pereima⁴¹, A. Pereiro Castro⁴⁶, P. Perret⁹, I. Petrenko⁵², M. Petric^{59,48},
 K. Petridis⁵⁴, A. Petrolini^{24,h}, A. Petrov⁸¹, S. Petrucci⁵⁸, M. Petruzzo²⁵, T.T.H. Pham⁶⁸,
 L. Pica^{29,m}, M. Piccini⁷⁸, B. Pietrzyk⁸, G. Pietrzyk⁴⁹, M. Pili⁶³, D. Pinci³⁰, F. Pisani⁴⁸,
 M. Pizzichemi⁴⁸, Resmi P.K.¹⁰, V. Placinta³⁷, J. Plews⁵³, M. Plo Casasus⁴⁶, F. Polci¹³,
 M. Poli Lener²³, M. Poliakova⁶⁸, A. Poluektov¹⁰, N. Polukhina^{83,u}, I. Polyakov⁶⁸, E. Polycarpo²,
 S. Ponce⁴⁸, D. Popov^{6,48}, S. Popov⁴², S. Poslavskii⁴⁴, K. Prasanth³⁵, L. Promberger⁴⁸,
 C. Prouve⁴⁶, V. Pugatch⁵², V. Puill¹¹, H. Pullen⁶³, G. Punzi^{29,n}, H. Qi³, W. Qian⁶, J. Qin⁶,
 N. Qin³, R. Quagliani^{13,54}, B. Quintana⁸, N.V. Raab¹⁸, R.I. Rabadan Trejo⁶, B. Rachwal³⁴,
 J.H. Rademacker⁵⁴, M. Rama²⁹, M. Ramos Pernas⁵⁶, M.S. Rangel², F. Ratnikov^{42,82},
 G. Raven³³, M. Reboud⁸, F. Redi⁴⁹, F. Reiss⁶², C. Remon Alepuz⁴⁷, Z. Ren³, V. Renaudin⁶³,
 R. Ribatti²⁹, S. Ricciardi⁵⁷, K. Rinnert⁶⁰, P. Robbe¹¹, G. Robertson⁵⁸, A.B. Rodrigues⁴⁹,
 E. Rodrigues⁶⁰, J.A. Rodriguez Lopez⁷⁴, E. Rodriguez Rodriguez⁴⁶, A. Rollings⁶³, P. Roloff⁴⁸,
 V. Romanovskiy⁴⁴, M. Romero Lamas⁴⁶, A. Romero Vidal⁴⁶, J.D. Roth⁸⁶, M. Rotondo²³,
 M.S. Rudolph⁶⁸, T. Ruf⁴⁸, R.A. Ruiz Fernandez⁴⁶, J. Ruiz Vidal⁴⁷, A. Ryzhikov⁸², J. Ryzka³⁴,
 J.J. Saborido Silva⁴⁶, N. Sagidova³⁸, N. Sahoo⁵⁶, B. Saitta^{27,e}, M. Salomoni⁴⁸,
 D. Sanchez Gonzalo⁴⁵, C. Sanchez Gras³², R. Santacesaria³⁰, C. Santamarina Rios⁴⁶,
 M. Santimaria²³, E. Santovetti^{31,p}, D. Saranin⁸³, G. Sarpis⁵⁹, M. Sarpis⁷⁵, A. Sarti³⁰,
 C. Satriano^{30,o}, A. Satta³¹, M. Saur¹⁵, D. Savrina^{41,40}, H. Sazak⁹, L.G. Scantlebury Smead⁶³,
 A. Scarabotto¹³, S. Schael¹⁴, S. Scherl⁶⁰, M. Schiller⁵⁹, H. Schindler⁴⁸, M. Schmelling¹⁶,
 B. Schmidt⁴⁸, S. Schmitt¹⁴, O. Schneider⁴⁹, A. Schopper⁴⁸, M. Schubiger³², S. Schulte⁴⁹,
 M.H. Schune¹¹, R. Schwemmer⁴⁸, B. Sciascia^{23,48}, S. Sellam⁴⁶, A. Semennikov⁴¹,
 M. Senghi Soares³³, A. Sergi²⁴, N. Serra⁵⁰, L. Sestini²⁸, A. Seuthe¹⁵, Y. Shang⁵,
 D.M. Shangase⁸⁶, M. Shapkin⁴⁴, I. Shchemerov⁸³, L. Shchutska⁴⁹, T. Shears⁶⁰,
 L. Shekhtman^{43,v}, Z. Shen⁵, V. Shevchenko⁸¹, E.B. Shields^{26,j}, Y. Shimizu¹¹, E. Shmanin⁸³,
 J.D. Shupperd⁶⁸, B.G. Siddi²¹, R. Silva Coutinho⁵⁰, G. Simi²⁸, S. Simone^{19,c}, N. Skidmore⁶²,
 T. Skwarnicki⁶⁸, M.W. Slater⁵³, I. Slazyk^{21,f}, J.C. Smallwood⁶³, J.G. Smeaton⁵⁵,
 A. Smetkina⁴¹, E. Smith⁵⁰, M. Smith⁶¹, A. Snoch³², M. Soares²⁰, L. Soares Lavra⁹,
 M.D. Sokoloff⁶⁵, F.J.P. Soler⁵⁹, A. Solovev³⁸, I. Solovyev³⁸, F.L. Souza De Almeida²,
 B. Souza De Paula², B. Spaan¹⁵, E. Spadaro Norella²⁵, P. Spradlin⁵⁹, F. Stagni⁴⁸, M. Stahl⁶⁵,
 S. Stahl⁴⁸, S. Stanislaus⁶³, O. Steinkamp^{50,83}, O. Stenyakin⁴⁴, H. Stevens¹⁵, S. Stone⁶⁸,
 M. Straticiu³⁷, D. Strelakina⁸³, F. Suljik⁶³, J. Sun²⁷, L. Sun⁷³, Y. Sun⁶⁶, P. Svihra⁶²,
 P.N. Swallow⁵³, K. Swientek³⁴, A. Szabelski³⁶, T. Szumlak³⁴, M. Szymanski⁴⁸, S. Taneja⁶²,
 A.R. Tanner⁵⁴, M.D. Tat⁶³, A. Terentev⁸³, F. Teubert⁴⁸, E. Thomas⁴⁸, D.J.D. Thompson⁵³,

K.A. Thomson⁶⁰, V. Tisserand⁹, S. T’Jampens⁸, M. Tobin⁴, L. Tomassetti^{21,f}, X. Tong⁵,
D. Torres Machado¹, D.Y. Tou¹³, M.T. Tran⁴⁹, E. Trifonova⁸³, C. Tripp⁴⁹, G. Tuci^{29,n},
A. Tully⁴⁹, N. Tuning^{32,48}, A. Ukleja³⁶, D.J. Unverzagt¹⁷, E. Ursov⁸³, A. Usachov³²,
A. Ustyuzhanin^{42,82}, U. Uwer¹⁷, A. Vagner⁸⁴, V. Vagnoni²⁰, A. Valassi⁴⁸, G. Valenti²⁰,
N. Valls Canudas⁸⁵, M. van Beuzekom³², M. Van Dijk⁴⁹, E. van Herwijnen⁸³, C.B. Van Hulse¹⁸,
M. van Veghel⁷⁹, R. Vazquez Gomez⁴⁶, P. Vazquez Regueiro⁴⁶, C. Vázquez Sierra⁴⁸, S. Vecchi²¹,
J.J. Velthuis⁵⁴, M. Veltri^{22,r}, A. Venkateswaran⁶⁸, M. Veronesi³², M. Vesterinen⁵⁶, D. Vieira⁶⁵,
M. Vieites Diaz⁴⁹, H. Viemann⁷⁶, X. Vilasis-Cardona⁸⁵, E. Vilella Figueras⁶⁰, A. Villa²⁰,
P. Vincent¹³, F.C. Volle¹¹, D. Vom Bruch¹⁰, A. Vorobyev³⁸, V. Vorobyev^{43,v}, N. Voropaev³⁸,
K. Vos⁸⁰, R. Waldi¹⁷, J. Walsh²⁹, C. Wang¹⁷, J. Wang⁵, J. Wang⁴, J. Wang³, J. Wang⁷³,
M. Wang³, R. Wang⁵⁴, Y. Wang⁷, Z. Wang⁵⁰, Z. Wang³, Z. Wang⁶, J.A. Ward⁵⁶,
N.K. Watson⁵³, S.G. Weber¹³, D. Websdale⁶¹, C. Weisser⁶⁴, B.D.C. Westhenry⁵⁴, D.J. White⁶²,
M. Whitehead⁵⁴, A.R. Wiederhold⁵⁶, D. Wiedner¹⁵, G. Wilkinson⁶³, M. Wilkinson⁶⁸,
I. Williams⁵⁵, M. Williams⁶⁴, M.R.J. Williams⁵⁸, F.F. Wilson⁵⁷, W. Wislicki³⁶, M. Witek³⁵,
L. Witola¹⁷, G. Wormser¹¹, S.A. Wotton⁵⁵, H. Wu⁶⁸, K. Wyllie⁴⁸, Z. Xiang⁶, D. Xiao⁷, Y. Xie⁷,
A. Xu⁵, J. Xu⁶, L. Xu³, M. Xu⁷, Q. Xu⁶, Z. Xu⁵, Z. Xu⁶, D. Yang³, S. Yang⁶, Y. Yang⁶,
Z. Yang⁵, Z. Yang⁶⁶, Y. Yao⁶⁸, L.E. Yeomans⁶⁰, H. Yin⁷, J. Yu⁷¹, X. Yuan⁶⁸, O. Yushchenko⁴⁴,
E. Zaffaroni⁴⁹, M. Zavertyaev^{16,u}, M. Zdybal³⁵, O. Zenaiev⁴⁸, M. Zeng³, D. Zhang⁷, L. Zhang³,
S. Zhang⁷¹, S. Zhang⁵, Y. Zhang⁵, Y. Zhang⁶³, A. Zharkova⁸³, A. Zhelezov¹⁷, Y. Zheng⁶,
T. Zhou⁵, X. Zhou⁶, Y. Zhou⁶, V. Zhovkovska¹¹, X. Zhu³, X. Zhu⁷, Z. Zhu⁶, V. Zhukov^{14,40},
J.B. Zonneveld⁵⁸, Q. Zou⁴, S. Zucchelli^{20,d}, D. Zuliani²⁸, G. Zunica⁶².

¹Centro Brasileiro de Pesquisas Físicas (CBPF), Rio de Janeiro, Brazil

²Universidade Federal do Rio de Janeiro (UFRJ), Rio de Janeiro, Brazil

³Center for High Energy Physics, Tsinghua University, Beijing, China

⁴Institute Of High Energy Physics (IHEP), Beijing, China

⁵School of Physics State Key Laboratory of Nuclear Physics and Technology, Peking University, Beijing, China

⁶University of Chinese Academy of Sciences, Beijing, China

⁷Institute of Particle Physics, Central China Normal University, Wuhan, Hubei, China

⁸Univ. Savoie Mont Blanc, CNRS, IN2P3-LAPP, Annecy, France

⁹Université Clermont Auvergne, CNRS/IN2P3, LPC, Clermont-Ferrand, France

¹⁰Aix Marseille Univ, CNRS/IN2P3, CPPM, Marseille, France

¹¹Université Paris-Saclay, CNRS/IN2P3, IJCLab, Orsay, France

¹²Laboratoire Leprince-Ringuet, CNRS/IN2P3, Ecole Polytechnique, Institut Polytechnique de Paris, Palaiseau, France

¹³LPNHE, Sorbonne Université, Paris Diderot Sorbonne Paris Cité, CNRS/IN2P3, Paris, France

¹⁴I. Physikalisches Institut, RWTH Aachen University, Aachen, Germany

¹⁵Fakultät Physik, Technische Universität Dortmund, Dortmund, Germany

¹⁶Max-Planck-Institut für Kernphysik (MPIK), Heidelberg, Germany

¹⁷Physikalisches Institut, Ruprecht-Karls-Universität Heidelberg, Heidelberg, Germany

¹⁸School of Physics, University College Dublin, Dublin, Ireland

¹⁹INFN Sezione di Bari, Bari, Italy

²⁰INFN Sezione di Bologna, Bologna, Italy

²¹INFN Sezione di Ferrara, Ferrara, Italy

²²INFN Sezione di Firenze, Firenze, Italy

²³INFN Laboratori Nazionali di Frascati, Frascati, Italy

²⁴INFN Sezione di Genova, Genova, Italy

²⁵INFN Sezione di Milano, Milano, Italy

²⁶INFN Sezione di Milano-Bicocca, Milano, Italy

²⁷INFN Sezione di Cagliari, Monserrato, Italy

²⁸Università degli Studi di Padova, Università e INFN, Padova, Padova, Italy

²⁹INFN Sezione di Pisa, Pisa, Italy

³⁰INFN Sezione di Roma La Sapienza, Roma, Italy

- ³¹ *INFN Sezione di Roma Tor Vergata, Roma, Italy*
- ³² *Nikhef National Institute for Subatomic Physics, Amsterdam, Netherlands*
- ³³ *Nikhef National Institute for Subatomic Physics and VU University Amsterdam, Amsterdam, Netherlands*
- ³⁴ *AGH - University of Science and Technology, Faculty of Physics and Applied Computer Science, Kraków, Poland*
- ³⁵ *Henryk Niewodniczanski Institute of Nuclear Physics Polish Academy of Sciences, Kraków, Poland*
- ³⁶ *National Center for Nuclear Research (NCBJ), Warsaw, Poland*
- ³⁷ *Horia Hulubei National Institute of Physics and Nuclear Engineering, Bucharest-Magurele, Romania*
- ³⁸ *Petersburg Nuclear Physics Institute NRC Kurchatov Institute (PNPI NRC KI), Gatchina, Russia*
- ³⁹ *Institute for Nuclear Research of the Russian Academy of Sciences (INR RAS), Moscow, Russia*
- ⁴⁰ *Institute of Nuclear Physics, Moscow State University (SINP MSU), Moscow, Russia*
- ⁴¹ *Institute of Theoretical and Experimental Physics NRC Kurchatov Institute (ITEP NRC KI), Moscow, Russia*
- ⁴² *Yandex School of Data Analysis, Moscow, Russia*
- ⁴³ *Budker Institute of Nuclear Physics (SB RAS), Novosibirsk, Russia*
- ⁴⁴ *Institute for High Energy Physics NRC Kurchatov Institute (IHEP NRC KI), Protvino, Russia, Protvino, Russia*
- ⁴⁵ *ICCUB, Universitat de Barcelona, Barcelona, Spain*
- ⁴⁶ *Instituto Galego de Física de Altas Enerxías (IGFAE), Universidade de Santiago de Compostela, Santiago de Compostela, Spain*
- ⁴⁷ *Instituto de Física Corpuscular, Centro Mixto Universidad de Valencia - CSIC, Valencia, Spain*
- ⁴⁸ *European Organization for Nuclear Research (CERN), Geneva, Switzerland*
- ⁴⁹ *Institute of Physics, Ecole Polytechnique Fédérale de Lausanne (EPFL), Lausanne, Switzerland*
- ⁵⁰ *Physik-Institut, Universität Zürich, Zürich, Switzerland*
- ⁵¹ *NSC Kharkiv Institute of Physics and Technology (NSC KIPT), Kharkiv, Ukraine*
- ⁵² *Institute for Nuclear Research of the National Academy of Sciences (KINR), Kyiv, Ukraine*
- ⁵³ *University of Birmingham, Birmingham, United Kingdom*
- ⁵⁴ *H.H. Wills Physics Laboratory, University of Bristol, Bristol, United Kingdom*
- ⁵⁵ *Cavendish Laboratory, University of Cambridge, Cambridge, United Kingdom*
- ⁵⁶ *Department of Physics, University of Warwick, Coventry, United Kingdom*
- ⁵⁷ *STFC Rutherford Appleton Laboratory, Didcot, United Kingdom*
- ⁵⁸ *School of Physics and Astronomy, University of Edinburgh, Edinburgh, United Kingdom*
- ⁵⁹ *School of Physics and Astronomy, University of Glasgow, Glasgow, United Kingdom*
- ⁶⁰ *Oliver Lodge Laboratory, University of Liverpool, Liverpool, United Kingdom*
- ⁶¹ *Imperial College London, London, United Kingdom*
- ⁶² *Department of Physics and Astronomy, University of Manchester, Manchester, United Kingdom*
- ⁶³ *Department of Physics, University of Oxford, Oxford, United Kingdom*
- ⁶⁴ *Massachusetts Institute of Technology, Cambridge, MA, United States*
- ⁶⁵ *University of Cincinnati, Cincinnati, OH, United States*
- ⁶⁶ *University of Maryland, College Park, MD, United States*
- ⁶⁷ *Los Alamos National Laboratory (LANL), Los Alamos, United States*
- ⁶⁸ *Syracuse University, Syracuse, NY, United States*
- ⁶⁹ *School of Physics and Astronomy, Monash University, Melbourne, Australia, associated to ⁵⁶*
- ⁷⁰ *Pontifícia Universidade Católica do Rio de Janeiro (PUC-Rio), Rio de Janeiro, Brazil, associated to ²*
- ⁷¹ *Physics and Micro Electronic College, Hunan University, Changsha City, China, associated to ⁷*
- ⁷² *Guangdong Provincial Key Laboratory of Nuclear Science, Guangdong-Hong Kong Joint Laboratory of Quantum Matter, Institute of Quantum Matter, South China Normal University, Guangzhou, China, associated to ³*
- ⁷³ *School of Physics and Technology, Wuhan University, Wuhan, China, associated to ³*
- ⁷⁴ *Departamento de Física, Universidad Nacional de Colombia, Bogota, Colombia, associated to ¹³*
- ⁷⁵ *Universität Bonn - Helmholtz-Institut für Strahlen und Kernphysik, Bonn, Germany, associated to ¹⁷*
- ⁷⁶ *Institut für Physik, Universität Rostock, Rostock, Germany, associated to ¹⁷*
- ⁷⁷ *Eotvos Lorand University, Budapest, Hungary, associated to ⁴⁸*
- ⁷⁸ *INFN Sezione di Perugia, Perugia, Italy, associated to ²¹*
- ⁷⁹ *Van Swinderen Institute, University of Groningen, Groningen, Netherlands, associated to ³²*

- ⁸⁰ *Universiteit Maastricht, Maastricht, Netherlands, associated to* ³²
⁸¹ *National Research Centre Kurchatov Institute, Moscow, Russia, associated to* ⁴¹
⁸² *National Research University Higher School of Economics, Moscow, Russia, associated to* ⁴²
⁸³ *National University of Science and Technology "MISIS", Moscow, Russia, associated to* ⁴¹
⁸⁴ *National Research Tomsk Polytechnic University, Tomsk, Russia, associated to* ⁴¹
⁸⁵ *DS4DS, La Salle, Universitat Ramon Llull, Barcelona, Spain, associated to* ⁴⁵
⁸⁶ *University of Michigan, Ann Arbor, United States, associated to* ⁶⁸

^a *Universidade Federal do Triângulo Mineiro (UFMT), Uberaba-MG, Brazil*

^b *Hangzhou Institute for Advanced Study, UCAS, Hangzhou, China*

^c *Università di Bari, Bari, Italy*

^d *Università di Bologna, Bologna, Italy*

^e *Università di Cagliari, Cagliari, Italy*

^f *Università di Ferrara, Ferrara, Italy*

^g *Università di Firenze, Firenze, Italy*

^h *Università di Genova, Genova, Italy*

ⁱ *Università degli Studi di Milano, Milano, Italy*

^j *Università di Milano Bicocca, Milano, Italy*

^k *Università di Modena e Reggio Emilia, Modena, Italy*

^l *Università di Padova, Padova, Italy*

^m *Scuola Normale Superiore, Pisa, Italy*

ⁿ *Università di Pisa, Pisa, Italy*

^o *Università della Basilicata, Potenza, Italy*

^p *Università di Roma Tor Vergata, Roma, Italy*

^q *Università di Siena, Siena, Italy*

^r *Università di Urbino, Urbino, Italy*

^s *MSU - Iligan Institute of Technology (MSU-IIT), Iligan, Philippines*

^t *AGH - University of Science and Technology, Faculty of Computer Science, Electronics and Telecommunications, Kraków, Poland*

^u *P.N. Lebedev Physical Institute, Russian Academy of Science (LPI RAS), Moscow, Russia*

^v *Novosibirsk State University, Novosibirsk, Russia*

^w *Department of Physics and Astronomy, Uppsala University, Uppsala, Sweden*

^x *Hanoi University of Science, Hanoi, Vietnam*